AIMS Mathematics, 11(8): 23687–23717
DOI:10.3934/math.2026954
Received: 09 May 2026
Revised: 23 July 2026
Accepted: 24 July 2026
Published: 03 August 2026

https://www.aimspress.com/journal/Math

Research article

A third-order fully decoupled relaxed E-SAV scheme for the hydrodynamically-coupled binary phase-field crystal model

Yue Shen[1], **Wenjie Wang**[1] **and Xiaoyue Xie**[2,*]

[1] School of Science, Xi'an University of Architecture and Technology, Xi'an 710055, China

[2] Equipment Management and Unmanned Aerial Vehicle Engineering School, Air Force Engineering University, Xi'an 710051, China

* **Correspondence:** Email: xxyueamss@163.com.

Abstract: This paper develops a third-order fully decoupled numerical scheme for the hydrodynamically-coupled binary phase-field crystal (BPFC) model based on the relaxed exponential scalar auxiliary variable (E-SAV) approach. The governing equations are derived from the L^2-gradient flow and coupled with the incompressible Navier-Stokes equations. To preserve total mass conservation, two nonlocal Lagrange multipliers are introduced into the chemical potentials. For temporal discretization, a third-order backward differentiation formula (BDF3) combined with explicit extrapolation techniques is adopted, leading to a linear and fully decoupled time-marching scheme. In addition, a relaxation strategy is incorporated into the E-SAV framework to improve the consistency between the modified energy and the original energy functional. Compared with existing second-order relaxed E-SAV schemes, the proposed method achieves higher temporal accuracy while retaining the advantages of linearity, decoupling, and energy stability. The proposed scheme only requires solving several linear elliptic equations with constant coefficients at each time step, making the algorithm computationally efficient and easy to implement. The unique solvability and discrete energy dissipation property of the numerical scheme are theoretically established. Furthermore, a consistency analysis is provided to show that the relaxation step preserves the third-order temporal accuracy of the primary variables and does not affect the overall convergence order of the scheme. Numerical experiments verify the expected third-order convergence rate, demonstrate the unconditional energy stability of the proposed scheme, and illustrate its effectiveness for long-time simulations of hydrodynamically-coupled crystal growth problems.

Keywords: hydrodynamically-coupled BPFC model; relaxed E-SAV method; BDF3 scheme; fully decoupled algorithm; energy stability
Mathematics Subject Classification: 35Q30, 65M06, 65M12, 76D05

1. Introduction

The phase-field crystal (PFC) model, originally proposed by Elder and co-workers [1,2], provides an efficient theoretical framework for describing phase transition dynamics and microstructure evolution at atomic length scales. In the PFC framework, a phase-field variable representing the averaged atomic density is introduced to characterize the microscopic structure of crystalline materials. The governing equations can then be derived through the variational formulation of the free energy functional. Due to its ability to capture elastic and plastic deformations of lattice structures as well as grain boundary dynamics, the PFC model has been widely applied in the simulation of crystal growth and related material evolution processes.

To improve the applicability of the PFC model in different physical scenarios, several extended models have been developed. One important extension is the modified phase-field crystal (MPFC) model, which incorporates elastic interaction effects to describe elastic relaxation processes. Another significant improvement introduces strongly nonlinear vacancy potentials into the free energy functional, enabling a more accurate description of point defects in crystalline materials. According to the number of components in the system, these models can be further classified into single-component PFC models, binary phase-field crystal (BPFC) models, and multi-component PFC models. In particular, the BPFC model employs two phase-field variables to characterize the local densities of two different atomic species. Compared with the single-component PFC model governed by a single evolution equation, the BPFC model contains additional coupling terms in the free energy functional, leading to a system of coupled partial differential equations.

In recent years, various structure-preserving numerical methods have achieved remarkable success in the simulation of dissipative systems, including the convex splitting method [3, 4], the scalar auxiliary variable (SAV) approach [5, 6], the invariant energy quadratization (IEQ) method [7, 8], the energy factorization (EF) method [9–11], which linearizes the energy functional while preserving the original energy dissipation, and several related structure-preserving techniques [12–14] for efficient and stable long-time simulations. Based on the convex splitting strategy of pseudo-energy, Wang and Wise [15] proposed an unconditionally energy-stable finite difference scheme for the MPFC model. Lee et al. [16] further developed first-order and second-order energy-stable schemes for the MPFC equation through suitable energy decomposition techniques. Liu and Li [17] constructed an unconditionally energy-stable numerical method for the PFC model based on a modified IEQ framework and established rigorous error estimates. By employing the SAV approach, Wang et al. [18] developed a second-order numerical scheme for the square PFC model and analyzed its optimal convergence rate. Li and Shen [19] proposed an efficient linear SAV scheme for the MPFC model that preserves mass conservation and unconditional pseudo-energy stability. In [20], a fully decoupled and energy-stable numerical method was developed for the BPFC model through the introduction of auxiliary variables. Based on the exponential scalar auxiliary variable (E-SAV) method, Zhang et al. [21] further constructed an energy-stable numerical scheme for the MPFC model with strongly nonlinear vacancy potentials.

Most of the aforementioned studies focus on PFC-type models derived from the H^{-1} gradient flow, which generally increases computational complexity and reduces computational efficiency. To address this issue, Lee [22] and related works [23, 24] considered PFC-type models based on the L^2 gradient flow. Meanwhile, nonlocal Lagrange multipliers were introduced to preserve the total mass

conservation property.

In practical crystallization processes, the influence of incompressible fluid flow is often non-negligible. Consequently, the PFC model is frequently coupled with the incompressible Navier-Stokes equations to describe crystal evolution in fluid environments. The introduction of hydrodynamic effects leads to strong coupling among phase-field variables, velocity fields, and pressure fields, which poses significant challenges in the design of efficient decoupled numerical algorithms. Moreover, many traditional structure-preserving methods become difficult to apply directly in the hydrodynamically-coupled setting, while auxiliary variable techniques have emerged as powerful tools for handling multi-variable coupling problems. In [25], a fully discrete decoupled finite element framework was proposed for the hydrodynamically-coupled PFC model by combining the IEQ method with additional auxiliary variables. Yang and He [26] developed a fully discrete linear finite element scheme with second-order temporal accuracy and decoupling structure for the flow-coupled BPFC system. However, the resulting scheme still involves relatively large computational costs and limited energy consistency. Subsequently, Yang and Kim [27] proposed a consistent energy-stable numerical method for the hydrodynamically-coupled PFC model based on the L^2 gradient flow, which improves computational efficiency while preserving energy consistency.

Recently, Wu et al. [28] developed a second-order relaxed E-SAV scheme for the hydrodynamically-coupled BPFC model based on the second-order backward differentiation formula (BDF2) discretization. Although the proposed method exhibits good stability and energy consistency properties, second-order temporal schemes may become insufficient for certain long-time evolution problems and multi-scale physical simulations. For example, in long-time crystal growth simulations, particle sedimentation processes, and coupled systems involving fast fluid motion and slow phase evolution, the accumulation of temporal discretization errors may significantly affect the reliability and accuracy of numerical results. Therefore, the development of higher-order temporal schemes is of both theoretical and practical importance.

Motivated by the above observations, in this work we further extend the relaxed E-SAV framework in [28] to third-order temporal accuracy. By combining the third-order backward differentiation formula (BDF3) with the E-SAV approach and relaxation strategy, we construct a new third-order fully decoupled and unconditionally energy-stable numerical scheme for the hydrodynamically-coupled BPFC model. Compared with the second-order scheme proposed in [28], the extension to third-order temporal discretization is nontrivial. In particular, the evolution equation of the auxiliary variable and the construction of the relaxation parameter must be carefully redesigned to preserve the discrete energy dissipation property while maintaining third-order temporal accuracy.

The main contributions of this work can be summarized as follows.

First, from the algorithmic point of view, a third-order relaxed E-SAV scheme is proposed for the hydrodynamically-coupled BPFC model. By combining the BDF3 discretization with explicit extrapolation techniques, the resulting numerical scheme remains linear and fully decoupled while achieving higher temporal accuracy.

Second, from the theoretical perspective, the unique solvability and discrete modified energy dissipation property of the proposed scheme are established. Furthermore, a consistency analysis is provided to show that the relaxation step preserves the third-order temporal accuracy of the primary variables.

Finally, numerical experiments are carried out to verify the expected third-order convergence rate

and demonstrate the stability and effectiveness of the proposed method through several representative crystal growth simulations. Compared with the second-order scheme, the proposed method can achieve higher accuracy under the same time step size, or equivalently allow larger time step sizes while maintaining comparable accuracy, thereby improving overall computational efficiency.

The remainder of this paper is organized as follows. In Section 2, the hydrodynamically-coupled BPFC model and its energy dissipation property are introduced. Section 3 presents the construction of the third-order fully decoupled numerical scheme together with the corresponding theoretical analysis. Numerical experiments are provided in Section 4 to demonstrate the effectiveness and stability of the proposed method. Finally, Section 5 draws some concluding remarks.

2. Mathematical formulation of the hydrodynamically-coupled BPFC model

In this section, we briefly introduce the mathematical formulation of the hydrodynamically-coupled BPFC model. The model describes the evolution of the local densities of two different atomic species coupled with an incompressible fluid flow. The formulation considered in this work is consistent with the hydrodynamically-coupled BPFC model proposed in [28], which serves as the foundation for the construction of the numerical scheme developed later.

2.1. Free energy functional and chemical potentials

Let $\Omega \subset \mathbb{R}^n$ $(n = 2, 3)$ be a bounded smooth domain. Denote by $\phi_1, \phi_2 : \Omega \to \mathbb{R}$ the local densities of two different atomic species, respectively. Following [28], the free energy functional of the system is given by

$$E(\phi_1, \phi_2) = \int_\Omega \lambda \left(\frac{1}{2}\phi_1 \mathcal{L}_1^2 \phi_1 + \frac{1}{2}\phi_2 \mathcal{L}_2^2 \phi_2 + \frac{1}{2}\phi_1 \mathcal{L}_{12}^2 \phi_2 + G(\phi_1, \phi_2) \right) d\boldsymbol{x}, \tag{2.1}$$

where $\lambda > 0$ is a constant and the differential operators $\mathcal{L}_1$, $\mathcal{L}_2$ and $\mathcal{L}_{12}$ are defined by

$$\mathcal{L}_1 = \Delta + a_1, \qquad \mathcal{L}_2 = \Delta + a_2, \qquad \mathcal{L}_{12} = \Delta + a_{12}. \tag{2.2}$$

Here, Δ denotes the Laplace operator, while the parameters a_1 and a_2 characterize the equilibrium distances between identical atomic species, and a_{12} characterizes the equilibrium distance between different atomic species.

The nonlinear potential $G(\phi_1, \phi_2)$ is defined as

$$G(\phi_1, \phi_2) := F_{dw}(\phi_1) + F_{dw}(\phi_2) + F_{vacancy}(\phi_1) + F_{vacancy}(\phi_2) + F_{coupling}(\phi_1, \phi_2), \tag{2.3}$$

where

$$F_{dw}(\phi) = \frac{1}{4}\phi^4 - \frac{\epsilon}{2}\phi^2, \qquad F_{vacancy}(\phi) = \frac{\alpha}{3}(|\phi|^3 - \phi^3),$$

and

$$F_{coupling}(\phi_1, \phi_2) = \frac{1}{2}\beta\phi_1^2\phi_2^2,$$

with $\epsilon, \alpha, \beta > 0$. The corresponding derivatives are given by

$$f_{dw}(\phi) = \phi^3 - \epsilon\phi, \tag{2.4}$$

$$f_{vacancy}(\phi) = \alpha(|\phi| - \phi)\phi, \tag{2.5}$$

$$f_{coupling,1}(\phi_1, \phi_2) = \beta\phi_1\phi_2^2, \tag{2.6}$$

$$f_{coupling,2}(\phi_1, \phi_2) = \beta\phi_1^2\phi_2. \tag{2.7}$$

Under periodic boundary conditions or homogeneous Neumann boundary conditions, the operators $\mathcal{L}_1$, $\mathcal{L}_2$, and $\mathcal{L}_{12}$ can be regarded as self-adjoint. Consequently, by taking the variational derivatives of the free energy functional $E(\phi_1, \phi_2)$ with respect to ϕ_1 and ϕ_2, respectively, the chemical potentials are obtained as

$$\mu_1 = \frac{\delta E}{\delta \phi_1} = \lambda\left(\mathcal{L}_1^2\phi_1 + \frac{1}{2}\mathcal{L}_{12}^2\phi_2 + g_1(\phi_1, \phi_2)\right), \tag{2.8}$$

$$\mu_2 = \frac{\delta E}{\delta \phi_2} = \lambda\left(\mathcal{L}_2^2\phi_2 + \frac{1}{2}\mathcal{L}_{12}^2\phi_1 + g_2(\phi_1, \phi_2)\right), \tag{2.9}$$

where

$$g_1(\phi_1, \phi_2) = \frac{\partial G}{\partial \phi_1} = \phi_1^3 - \epsilon\phi_1 + \alpha(|\phi_1| - \phi_1)\phi_1 + \beta\phi_1\phi_2^2, \tag{2.10}$$

$$g_2(\phi_1, \phi_2) = \frac{\partial G}{\partial \phi_2} = \phi_2^3 - \epsilon\phi_2 + \alpha(|\phi_2| - \phi_2)\phi_2 + \beta\phi_1^2\phi_2. \tag{2.11}$$

2.2. Mass conservation correction

By employing the L^2 gradient flow, the governing equations can be written as

$$\phi_{1t} = -M\mu_1, \tag{2.12}$$

$$\mu_1 = \lambda\left(\mathcal{L}_1^2\phi_1 + \frac{1}{2}\mathcal{L}_{12}^2\phi_2 + g_1(\phi_1, \phi_2)\right), \tag{2.13}$$

$$\phi_{2t} = -M\mu_2, \tag{2.14}$$

$$\mu_2 = \lambda\left(\mathcal{L}_2^2\phi_2 + \frac{1}{2}\mathcal{L}_{12}^2\phi_1 + g_2(\phi_1, \phi_2)\right). \tag{2.15}$$

Here, $M > 0$ denotes the mobility coefficient. We consider the following boundary conditions:

$$\mathbf{n} \cdot \nabla\phi_1|_{\partial\Omega} = \mathbf{n} \cdot \nabla\phi_2|_{\partial\Omega} = \mathbf{n} \cdot \nabla\Delta\phi_1|_{\partial\Omega} = \mathbf{n} \cdot \nabla\Delta\phi_2|_{\partial\Omega} = 0, \tag{2.16}$$

where $\mathbf{n}$ denotes the unit outward normal vector on the boundary $\partial\Omega$. These boundary conditions guarantee the zero-flux property of the Laplace operator in the integral sense.

Taking the time derivative of the total mass and applying the divergence theorem yields

$$\frac{d}{dt}\int_\Omega \phi_1 d\boldsymbol{x} = \int_\Omega \phi_{1t} d\boldsymbol{x} = -M\int_\Omega \mu_1 d\boldsymbol{x}. \tag{2.17}$$

Using (2.13) together with the boundary condition (2.16), the Laplacian terms vanish after integration, and thus

$$\frac{d}{dt}\int_\Omega \phi_1 d\boldsymbol{x} = -M\lambda\int_\Omega \left(a_1^2\phi_1 + \frac{1}{2}a_{12}^2\phi_2 + g_1(\phi_1, \phi_2)\right) d\boldsymbol{x} \neq 0. \tag{2.18}$$

Similarly, one obtains

$$\frac{d}{dt}\int_\Omega \phi_2 d\boldsymbol{x} = -M\lambda \int_\Omega \left(a_2^2\phi_2 + \frac{1}{2}a_{12}^2\phi_1 + g_2(\phi_1,\phi_2)\right) d\boldsymbol{x} \neq 0. \tag{2.19}$$

Therefore, the original system generally does not preserve mass conservation.

To enforce mass conservation, namely,

$$\frac{d}{dt}\int_\Omega \phi_1 d\boldsymbol{x} = \frac{d}{dt}\int_\Omega \phi_2 d\boldsymbol{x} = 0,$$

we follow the approach in [23, 28] and introduce the following nonlocal Lagrange multipliers:

$$H_1(\phi_1,\phi_2) = \frac{1}{|\Omega|}\int_\Omega \left(a_1^2\phi_1 + \frac{1}{2}a_{12}^2\phi_2 + g_1(\phi_1,\phi_2)\right) d\boldsymbol{x}, \tag{2.20}$$

$$H_2(\phi_1,\phi_2) = \frac{1}{|\Omega|}\int_\Omega \left(a_2^2\phi_2 + \frac{1}{2}a_{12}^2\phi_1 + g_2(\phi_1,\phi_2)\right) d\boldsymbol{x}, \tag{2.21}$$

where

$$|\Omega| = \int_\Omega 1\, d\boldsymbol{x}.$$

By incorporating the above Lagrange multipliers into the chemical potentials, the modified system becomes

$$\phi_{1t} = -M\mu_1, \tag{2.22}$$

$$\mu_1 = \lambda\left(\mathcal{L}_1^2\phi_1 + \frac{1}{2}\mathcal{L}_{12}^2\phi_2 + g_1(\phi_1,\phi_2) - H_1(\phi_1,\phi_2)\right), \tag{2.23}$$

$$\phi_{2t} = -M\mu_2, \tag{2.24}$$

$$\mu_2 = \lambda\left(\mathcal{L}_2^2\phi_2 + \frac{1}{2}\mathcal{L}_{12}^2\phi_1 + g_2(\phi_1,\phi_2) - H_2(\phi_1,\phi_2)\right). \tag{2.25}$$

The mass conservation property can now be verified directly. Taking ϕ_1 as an example, it follows from (2.22) that

$$\begin{aligned}\frac{d}{dt}\int_\Omega \phi_1 d\boldsymbol{x} &= \int_\Omega \phi_{1t} d\boldsymbol{x} = -M\int_\Omega \mu_1 d\boldsymbol{x} \\ &= -M\lambda\int_\Omega \left(a_1^2\phi_1 + \frac{1}{2}a_{12}^2\phi_2 + g_1(\phi_1,\phi_2)\right) d\boldsymbol{x} + M\lambda|\Omega|H_1(\phi_1,\phi_2).\end{aligned} \tag{2.26}$$

By the definition of H_1, the right-hand side vanishes, which implies

$$\frac{d}{dt}\int_\Omega \phi_1 d\boldsymbol{x} = 0. \tag{2.27}$$

Similarly, one obtains

$$\frac{d}{dt}\int_\Omega \phi_2 d\boldsymbol{x} = 0. \tag{2.28}$$

Hence, the modified system preserves the total mass conservation property.

2.3. Hydrodynamically-coupled model

In practical physical processes, crystallization usually occurs in fluid environments, and its evolution dynamics are significantly influenced by the surrounding flow field. To more accurately describe such phenomena, we follow the approach in [28] and couple the above BPFC model with the incompressible Navier-Stokes equations, resulting in the following hydrodynamically-coupled system:

$$\mathbf{u}_t + \mathbf{u}\cdot\nabla\mathbf{u} + \nabla p = \frac{1}{Re}\Delta\mathbf{u} - \phi_1\nabla\mu_1 - \phi_2\nabla\mu_2, \tag{2.29}$$

$$\nabla\cdot\mathbf{u} = 0, \tag{2.30}$$

$$\phi_{1t} + \nabla\cdot(\mathbf{u}\phi_1) = -M\mu_1, \tag{2.31}$$

$$\mu_1 = \lambda\left(\mathcal{L}_1^2\phi_1 + \frac{1}{2}\mathcal{L}_{12}^2\phi_2 - H_1(\phi_1,\phi_2) + g_1(\phi_1,\phi_2)\right), \tag{2.32}$$

$$\phi_{2t} + \nabla\cdot(\mathbf{u}\phi_2) = -M\mu_2, \tag{2.33}$$

$$\mu_2 = \lambda\left(\mathcal{L}_2^2\phi_2 + \frac{1}{2}\mathcal{L}_{12}^2\phi_1 - H_2(\phi_1,\phi_2) + g_2(\phi_1,\phi_2)\right). \tag{2.34}$$

Here, $\mathbf{u}$ denotes the velocity field, p is the pressure, and Re represents the Reynolds number, where $1/Re$ corresponds to the dimensionless viscosity coefficient. The coupling terms $-\phi_i\nabla\mu_i$ describe the body forces exerted by the phase fields on the fluid.

Since the incompressibility condition

$$\nabla\cdot\mathbf{u} = 0$$

holds, the convective terms in the phase-field equations are written in the conservative form

$$\nabla\cdot(\mathbf{u}\phi_i).$$

Periodic boundary conditions may be imposed. Alternatively, one may consider the following homogeneous boundary conditions:

$$\mathbf{n}\cdot\nabla\phi_1|_{\partial\Omega} = \mathbf{n}\cdot\nabla\phi_2|_{\partial\Omega} = \mathbf{n}\cdot\nabla\Delta\phi_1|_{\partial\Omega} = \mathbf{n}\cdot\nabla\Delta\phi_2|_{\partial\Omega} = 0, \qquad \mathbf{u}|_{\partial\Omega} = \mathbf{0}. \tag{2.35}$$

2.4. Energy dissipation law

To show that the system satisfies an energy dissipation property, we define the total energy functional by

$$E(\mathbf{u},\phi_1,\phi_2) = \int_\Omega\left(\frac{1}{2}|\mathbf{u}|^2 + \lambda\left(\frac{1}{2}\phi_1\mathcal{L}_1^2\phi_1 + \frac{1}{2}\phi_2\mathcal{L}_2^2\phi_2 + \frac{1}{2}\phi_1\mathcal{L}_{12}^2\phi_2 + G(\phi_1,\phi_2)\right)\right)d\boldsymbol{x}. \tag{2.36}$$

Taking the L^2 inner product of (2.31) with μ_1 and the inner product of (2.32) with ϕ_{1t}, proceeding similarly for (2.33) and (2.34), then summing all resulting equations together, one obtains

$$\begin{aligned}&\frac{d}{dt}\int_\Omega\lambda\left(\frac{1}{2}\phi_1\mathcal{L}_1^2\phi_1 + \frac{1}{2}\phi_2\mathcal{L}_2^2\phi_2 + \frac{1}{2}\phi_1\mathcal{L}_{12}^2\phi_2 + G(\phi_1,\phi_2)\right)d\boldsymbol{x}\\ &= -M\|\mu_1\|^2 - M\|\mu_2\|^2 - (\nabla\cdot(\mathbf{u}\phi_1),\mu_1) - (\nabla\cdot(\mathbf{u}\phi_2),\mu_2) + H_1(\phi_1,\phi_2)(\phi_{1t},1) + H_2(\phi_1,\phi_2)(\phi_{2t},1).\end{aligned} \tag{2.37}$$

Here and below, $(\cdot,\cdot)$ and $\|\cdot\|$ denote the standard $L^2(\Omega)$-inner product and norm, respectively, given by

$$(u,v)=\int_\Omega uv\,dx,\qquad \|u\|=(u,u)^{1/2}.$$

From the mass conservation relations (2.27)-(2.28), we have

$$(\phi_{1t},1)=0,\qquad (\phi_{2t},1)=0,$$

and therefore the last two terms in (2.37) vanish.

Next, taking the L^2 inner product of (2.29) with $\mathbf{u}$ and using the incompressibility condition

$$\nabla\cdot\mathbf{u}=0,$$

together with the identities

$$(\mathbf{u}\cdot\nabla\mathbf{u},\mathbf{u})=0,\qquad (\nabla p,\mathbf{u})=0,$$

yields

$$\frac{d}{dt}\int_\Omega\frac{1}{2}|\mathbf{u}|^2d\boldsymbol{x}=-(\phi_1\nabla\mu_1,\mathbf{u})-(\phi_2\nabla\mu_2,\mathbf{u})-\frac{1}{Re}\|\nabla\mathbf{u}\|^2. \tag{2.38}$$

Adding (2.37) and (2.38) and using the identity

$$(\nabla\cdot(\mathbf{u}\phi),\mu)=-(\phi\nabla\mu,\mathbf{u}),$$

which holds under periodic boundary conditions or the homogeneous boundary conditions (2.35), we finally obtain the following energy dissipation law:

$$\frac{d}{dt}E(\mathbf{u},\phi_1,\phi_2)=-M\|\mu_1\|^2-M\|\mu_2\|^2-\frac{1}{Re}\|\nabla\mathbf{u}\|^2\le 0. \tag{2.39}$$

The above result shows that the hydrodynamically-coupled BPFC model satisfies an energy dissipation structure, which provides an important theoretical foundation for the construction and stability analysis of the numerical schemes developed later. Based on this model, a third-order temporal discretization scheme will be proposed in Section 3.

3. A third-order fully decoupled BDF3 scheme

In this section, we construct a third-order fully decoupled temporal discretization scheme for the hydrodynamically-coupled BPFC model based on the BDF3 approach. Let

$$\Delta t=\frac{T}{N},\qquad t^n=n\Delta t,$$

and denote by ψ^n the numerical approximation of ψ at time t^n. To preserve the linearized and decoupled structure of the numerical scheme, we introduce the following third-order explicit extrapolation:

$$\psi^*=3\psi^n-3\psi^{n-1}+\psi^{n-2}. \tag{3.1}$$

Meanwhile, to construct the E-SAV formulation, we introduce the exponential scalar auxiliary variable

$$V(t) = \exp\left(\frac{1}{C}E(\mathbf{u}, \phi_1, \phi_2)\right), \tag{3.2}$$

where $C > 0$ is a prescribed constant.

At the discrete level, the modified energy associated with the auxiliary variable V is naturally defined as

$$\mathcal{E}^n = C \ln V^n. \tag{3.3}$$

The discrete dissipation property of this modified energy will be rigorously established in Theorem 3.3 below.

Applying the BDF3 discretization to the temporal derivatives, we first solve the velocity prediction equation

$$\frac{11\tilde{\mathbf{u}}^{n+1} - 18\mathbf{u}^n + 9\mathbf{u}^{n-1} - 2\mathbf{u}^{n-2}}{6\Delta t} + \mathbf{u}^* \cdot \nabla \mathbf{u}^* + \nabla p^n = \frac{1}{Re}\Delta \tilde{\mathbf{u}}^{n+1} - \sum_{i=1}^{2} \phi_i^* \nabla \mu_i^*. \tag{3.4}$$

Next, the pressure correction step is performed:

$$\frac{11\hat{\mathbf{u}}^{n+1} - 11\tilde{\mathbf{u}}^{n+1}}{6\Delta t} + \nabla(p^{n+1} - p^n) = \mathbf{0}, \tag{3.5}$$

that is,

$$\hat{\mathbf{u}}^{n+1} = \tilde{\mathbf{u}}^{n+1} - \frac{6\Delta t}{11}\nabla(p^{n+1} - p^n). \tag{3.6}$$

The corrected velocity field satisfies the incompressibility condition

$$\nabla \cdot \hat{\mathbf{u}}^{n+1} = 0. \tag{3.7}$$

Combining (3.5) and (3.7), we obtain the pressure Poisson equation

$$\Delta(p^{n+1} - p^n) = \frac{11}{6\Delta t}\nabla \cdot \tilde{\mathbf{u}}^{n+1}. \tag{3.8}$$

The intermediate phase-field variables are determined by the following linear systems:

$$\frac{11\hat{\phi}_1^{n+1} - 18\phi_1^n + 9\phi_1^{n-1} - 2\phi_1^{n-2}}{6\Delta t} + \nabla \cdot (\mathbf{u}^* \phi_1^*) = -M\mu_1^{n+1}, \tag{3.9}$$

where

$$\mu_1^{n+1} = \lambda\left(\mathcal{L}_1^2\hat{\phi}_1^{n+1} + \frac{1}{2}\mathcal{L}_{12}^2\phi_2^* - H_1(\phi_1^*, \phi_2^*) + g_1(\phi_1^*, \phi_2^*) + S(\hat{\phi}_1^{n+1} - \phi_1^*)\right), \tag{3.10}$$

and

$$\frac{11\hat{\phi}_2^{n+1} - 18\phi_2^n + 9\phi_2^{n-1} - 2\phi_2^{n-2}}{6\Delta t} + \nabla \cdot (\mathbf{u}^* \phi_2^*) = -M\mu_2^{n+1}, \tag{3.11}$$

where

$$\mu_2^{n+1} = \lambda\left(\mathcal{L}_2^2\hat{\phi}_2^{n+1} + \frac{1}{2}\mathcal{L}_{12}^2\phi_1^* - H_2(\phi_1^*, \phi_2^*) + g_2(\phi_1^*, \phi_2^*) + S(\hat{\phi}_2^{n+1} - \phi_2^*)\right). \tag{3.12}$$

Here, $S > 0$ denotes the stabilization parameter.

To describe the evolution of the modified energy, we further introduce the exponential scalar auxiliary variable V. We first compute the intermediate auxiliary variable $\tilde{V}^{n+1}$ through

$$\frac{\tilde{V}^{n+1} - V^n}{\Delta t} = -\frac{1}{C}\tilde{V}^{n+1}\left(\frac{1}{Re}\|\nabla \mathbf{u}^*\|^2 + M\|\mu_1^*\|^2 + M\|\mu_2^*\|^2\right), \tag{3.13}$$

which leads to the explicit formula

$$\tilde{V}^{n+1} = \frac{V^n}{1 + \frac{\Delta t}{C}\left(\frac{1}{Re}\|\nabla \mathbf{u}^*\|^2 + M\|\mu_1^*\|^2 + M\|\mu_2^*\|^2\right)}. \tag{3.14}$$

Here, $C > 0$ is a prescribed constant, and μ_i^* denotes the explicit extrapolation of the chemical potentials.

3.1. Relaxation step and variable update

To improve the consistency between the auxiliary variable and the original energy functional, we adopt the relaxation strategy proposed in [28] and define

$$\xi^{n+1} = \tilde{V}^{n+1}\exp\left(-\frac{1}{C}E(\mathbf{u}^*, \phi_1^*, \phi_2^*)\right). \tag{3.15}$$

The final physical variables are then updated through the correction factor $\xi^{n+1}(2 - \xi^{n+1})$:

$$\phi_1^{n+1} = \xi^{n+1}(2 - \xi^{n+1})\hat{\phi}_1^{n+1}, \tag{3.16}$$

$$\phi_2^{n+1} = \xi^{n+1}(2 - \xi^{n+1})\hat{\phi}_2^{n+1}, \tag{3.17}$$

$$\mathbf{u}^{n+1} = \xi^{n+1}(2 - \xi^{n+1})\hat{\mathbf{u}}^{n+1}. \tag{3.18}$$

Since ξ^{n+1} only depends on time and is independent of the spatial variables, the divergence-free property is preserved. More precisely, if

$$\nabla \cdot \hat{\mathbf{u}}^{n+1} = 0,$$

then the corrected velocity field still satisfies

$$\nabla \cdot \mathbf{u}^{n+1} = 0.$$

We further define

$$\overline{V}^{n+1} = \exp\left(\frac{1}{C}E(\mathbf{u}^{n+1}, \phi_1^{n+1}, \phi_2^{n+1})\right). \tag{3.19}$$

The final auxiliary variable V^{n+1} is determined through the relaxation step

$$V^{n+1} = \sigma_0\tilde{V}^{n+1} + (1 - \sigma_0)\overline{V}^{n+1}, \qquad 0 \le \sigma_0 \le 1, \tag{3.20}$$

where the parameter σ_0 is chosen according to the relaxation strategy proposed in [28] so that the modified energy preserves the discrete dissipation property.

It should be emphasized that the correction formulas (3.16)–(3.18) were originally introduced for BDF2 schemes. For the present BDF3 discretization, we next show from the consistency viewpoint that the relaxation correction step does not reduce the third-order temporal accuracy of the primary variables.

Lemma 3.1. *Assume that the intermediate variables satisfy*

$$\hat{\phi}_i^{n+1} = \phi_i(t^{n+1}) + O(\Delta t^3), \qquad i = 1, 2, \qquad \hat{\mathbf{u}}^{n+1} = \mathbf{u}(t^{n+1}) + O(\Delta t^3), \tag{3.21}$$

and the auxiliary variable together with the explicit extrapolated quantities satisfy

$$\tilde{V}^{n+1} = V(t^{n+1}) + O(\Delta t^3), \tag{3.22}$$

$$\mathbf{u}^* = \mathbf{u}(t^{n+1}) + O(\Delta t^3), \tag{3.23}$$

$$\phi_i^* = \phi_i(t^{n+1}) + O(\Delta t^3), \qquad i = 1, 2. \tag{3.24}$$

Then the final corrected variables obtained from (3.16)–(3.18) *still satisfy*

$$\phi_i^{n+1} = \phi_i(t^{n+1}) + O(\Delta t^3), \qquad i = 1, 2, \qquad \mathbf{u}^{n+1} = \mathbf{u}(t^{n+1}) + O(\Delta t^3). \tag{3.25}$$

Proof. From (3.15), we have

$$\xi^{n+1} = \tilde{V}^{n+1} \exp\left(-\frac{1}{C} E(\mathbf{u}^*, \phi_1^*, \phi_2^*)\right). \tag{3.26}$$

Assume that the exact solution is sufficiently smooth and bounded over the considered time interval. Since the exponential function is smooth on bounded intervals, it follows from (3.23)-(3.24) that

$$\exp\left(-\frac{1}{C} E(\mathbf{u}^*, \phi_1^*, \phi_2^*)\right) = \exp\left(-\frac{1}{C} E(t^{n+1})\right) + O(\Delta t^3). \tag{3.27}$$

Moreover, from the definition of the auxiliary variable (3.2), we have

$$V(t^{n+1}) = \exp\left(\frac{1}{C} E(t^{n+1})\right), \tag{3.28}$$

which implies

$$V(t^{n+1}) \exp\left(-\frac{1}{C} E(t^{n+1})\right) = 1. \tag{3.29}$$

Substituting (3.22) and (3.27) into (3.26) and using (3.29), we obtain

$$\xi^{n+1} = 1 + O(\Delta t^3). \tag{3.30}$$

Denote

$$\varepsilon^{n+1} = \xi^{n+1} - 1.$$

Then

$$\varepsilon^{n+1} = O(\Delta t^3).$$

Consequently,

$$\xi^{n+1}(2 - \xi^{n+1}) = (1 + \varepsilon^{n+1})(1 - \varepsilon^{n+1}) = 1 - (\varepsilon^{n+1})^2 = 1 + O(\Delta t^6). \tag{3.31}$$

Using (3.16)–(3.18), together with the boundedness of the intermediate solutions, we further obtain

$$\phi_i^{n+1} = \left(1 + O(\Delta t^6)\right) \hat{\phi}_i^{n+1} = \phi_i(t^{n+1}) + O(\Delta t^3), \qquad i = 1, 2, \tag{3.32}$$

$$\mathbf{u}^{n+1} = \left(1 + O(\Delta t^6)\right) \hat{\mathbf{u}}^{n+1} = \mathbf{u}(t^{n+1}) + O(\Delta t^3). \tag{3.33}$$

Therefore, the relaxation correction step does not reduce the third-order temporal accuracy of the primary variables.

3.2. Algorithmic procedure

Since the BDF3 scheme is a three-step multistep method, numerical solutions at the first three time levels are required for initialization. The initialization procedure is summarized as follows:

- At $n = 0$, the initial conditions directly provide $\mathbf{u}^0$, ϕ_1^0, and ϕ_2^0, and the auxiliary variable V^0 is computed through (3.2);
- At $n = 1$, a first-order backward differentiation formula (BDF1) scheme is employed to advance the solution from $n = 0$ and obtain $\mathbf{u}^1$, ϕ_1^1, ϕ_2^1, and V^1;
- At $n = 2$, a BDF2 scheme is applied using the solutions at $n = 0, 1$ to compute $\mathbf{u}^2$, ϕ_1^2, ϕ_2^2, and V^2.

After the initialization process, for any $n \geq 2$, each time step is advanced according to Algorithm 1.

Algorithm 1 One-step procedure of the relaxed E-SAV BDF3 scheme

1: Compute $\tilde{V}^{n+1}$ explicitly from (3.13);
2: Solve (3.9)-(3.10) to obtain $\hat{\phi}_1^{n+1}$ and μ_1^{n+1};
3: Solve (3.11)-(3.12) to obtain $\hat{\phi}_2^{n+1}$ and μ_2^{n+1};
4: Solve (3.4) to obtain the intermediate velocity $\tilde{\mathbf{u}}^{n+1}$;
5: Construct and solve the pressure Poisson equation from (3.5) and (3.7) to obtain p^{n+1};
6: Compute the corrected velocity $\hat{\mathbf{u}}^{n+1}$ through (3.6);
7: Compute ξ^{n+1} from (3.15), and update the auxiliary variable V^{n+1} through the relaxation step (3.20);
8: Update the final physical variables ϕ_1^{n+1}, ϕ_2^{n+1}, and $\mathbf{u}^{n+1}$ through (3.16)–(3.18).

3.3. Theoretical analysis

Theorem 3.2. *(Unique solvability) At each time step, the variables $\tilde{V}^{n+1}$, $\hat{\phi}_1^{n+1}$, $\hat{\phi}_2^{n+1}$, $\tilde{\mathbf{u}}^{n+1}$, $\hat{\mathbf{u}}^{n+1}$, p^{n+1}, and V^{n+1} defined by* (3.4)–(3.12) *together with the relaxation step are uniquely determined.*

Proof. First, from (3.13), we have

$$\tilde{V}^{n+1} = \frac{V^n}{1 + \frac{\Delta t}{C}\left(\frac{1}{Re}\|\nabla \mathbf{u}^*\|^2 + M\|\mu_1^*\|^2 + M\|\mu_2^*\|^2\right)}.$$

Since $V^n > 0$ is known and the denominator is strictly positive, $\tilde{V}^{n+1}$ is uniquely determined. Furthermore, ξ^{n+1} is uniquely determined from (3.15). After obtaining the final physical variables, $\overline{V}^{n+1}$ is uniquely determined by (3.19), and consequently V^{n+1} is uniquely determined through the relaxation formula (3.20).

Next, consider the intermediate phase-field variable $\hat{\phi}_1^{n+1}$. Substituting (3.10) into (3.9) yields the following linear elliptic equation:

$$\left(\frac{11}{6\Delta t} + M\lambda S\right)\hat{\phi}_1^{n+1} + M\lambda \mathcal{L}_1^2 \hat{\phi}_1^{n+1} + f_1^{n,n-1,n-2} = 0, \tag{3.34}$$

where $f_1^{n,n-1,n-2}$ only depends on known quantities.

To prove uniqueness, we introduce the functional

$$F_1(\phi) = \int_\Omega \left[\frac{1}{2}\left(\frac{11}{6\Delta t} + M\lambda S \right)\phi^2 + \frac{1}{2} M\lambda \phi \mathcal{L}_1^2 \phi + f_1^{n,n-1,n-2}\phi \right] d\boldsymbol{x}. \tag{3.35}$$

Under the imposed boundary conditions, the operator $\mathcal{L}_1$ is self-adjoint and satisfies

$$\int_\Omega \phi \mathcal{L}_1^2 \phi \, d\boldsymbol{x} = \int_\Omega \left((\Delta + a_1)\phi \right)^2 d\boldsymbol{x}.$$

Therefore, for any nonzero perturbation ψ, we have

$$\frac{d^2}{dl^2} F_1(\phi + l\psi)\bigg|_{l=0} = \int_\Omega \left[\left(\frac{11}{6\Delta t} + M\lambda S \right)\psi^2 + M\lambda \left((\Delta + a_1)\psi \right)^2 \right] d\boldsymbol{x} > 0.$$

Hence, F_1 is strictly convex and admits a unique minimizer, which implies that (3.34) has a unique solution. By the same argument, $\hat{\phi}_2^{n+1}$ is also uniquely determined.

Next, from (3.4), the intermediate velocity satisfies

$$\left(\frac{11}{6\Delta t} - \frac{1}{Re}\Delta \right) \tilde{\mathbf{u}}^{n+1} = \mathbf{R}^n, \tag{3.36}$$

where $\mathbf{R}^n$ only depends on known quantities. Since the operator

$$\frac{11}{6\Delta t} - \frac{1}{Re}\Delta$$

is a positive definite elliptic operator under periodic or homogeneous boundary conditions, $\tilde{\mathbf{u}}^{n+1}$ uniquely exists.

Combining (3.5) and the incompressibility condition (3.7) yields the pressure Poisson equation

$$\Delta(p^{n+1} - p^n) = \frac{11}{6\Delta t} \nabla \cdot \tilde{\mathbf{u}}^{n+1}.$$

Under the corresponding Neumann boundary condition, the pressure is unique up to an additive constant. Imposing the zero-average condition

$$\int_\Omega p^{n+1} \, d\boldsymbol{x} = 0$$

guarantees the uniqueness of p^{n+1}. Consequently, $\hat{\mathbf{u}}^{n+1}$ is uniquely determined through (3.6).

Finally, the final physical variables ϕ_1^{n+1}, ϕ_2^{n+1}, and $\mathbf{u}^{n+1}$ are uniquely determined from (3.16)–(3.18). Therefore, all variables are uniquely determined at each time step.

Theorem 3.3. *(Discrete dissipation of the modified energy $\mathcal{E}^n = C \ln V^n$) Assume that*

$$V^0 = \exp\left(\frac{1}{C} E(\mathbf{u}^0, \phi_1^0, \phi_2^0) \right) > 0.$$

The unconditional energy stability of the proposed scheme is established for the modified energy $\mathcal{E}^n = C \ln V^n$, which is a standard feature of the E-SAV approach. The consistency between this modified energy and the original physical energy $E(\mathbf{u}, \phi_1, \phi_2)$ is numerically verified in Section 4.2 (see Figure 2 and the related discussion). Let the relaxation parameter $\sigma_0 \in [0, 1]$ and the auxiliary parameter $\gamma^{n+1} \geq 0$ be chosen according to the following strategy [28]:

- *If* $\tilde{V}^{n+1} = \overline{V}^{n+1}$, *set* $\sigma_0 = 0$ *and*

$$\gamma^{n+1} = \frac{\tilde{V}^{n+1}\left(\frac{1}{Re}\|\nabla \mathbf{u}^n\|^2 + M\|\mu_1^n\|^2 + M\|\mu_2^n\|^2\right)}{C\left(\frac{1}{Re}\|\nabla \mathbf{u}^{n+1}\|^2 + M\|\mu_1^{n+1}\|^2 + M\|\mu_2^{n+1}\|^2\right)}.$$

- *If* $\tilde{V}^{n+1} > \overline{V}^{n+1}$, *set* $\sigma_0 = 0$ *and*

$$\gamma^{n+1} = \frac{\tilde{V}^{n+1} - \overline{V}^{n+1}}{\delta t\left(\frac{1}{Re}\|\nabla \mathbf{u}^{n+1}\|^2 + M\|\mu_1^{n+1}\|^2 + M\|\mu_2^{n+1}\|^2\right)} + \frac{\tilde{V}^{n+1}\left(\frac{1}{Re}\|\nabla \mathbf{u}^n\|^2 + M\|\mu_1^n\|^2 + M\|\mu_2^n\|^2\right)}{C\left(\frac{1}{Re}\|\nabla \mathbf{u}^{n+1}\|^2 + M\|\mu_1^{n+1}\|^2 + M\|\mu_2^{n+1}\|^2\right)}.$$

- *If* $\tilde{V}^{n+1} < \overline{V}^{n+1}$ *and*

$$\tilde{V}^{n+1} - \overline{V}^{n+1} + \frac{\delta t}{C}\tilde{V}^{n+1}\left(\frac{1}{Re}\|\nabla \mathbf{u}^n\|^2 + M\|\mu_1^n\|^2 + M\|\mu_2^n\|^2\right) \geq 0,$$

  set $\sigma_0 = 0$ *and keep* γ^{n+1} *as in the previous case.*

- *If* $\tilde{V}^{n+1} < \overline{V}^{n+1}$ *and*

$$\tilde{V}^{n+1} - \overline{V}^{n+1} + \frac{\delta t}{C}\tilde{V}^{n+1}\left(\frac{1}{Re}\|\nabla \mathbf{u}^n\|^2 + M\|\mu_1^n\|^2 + M\|\mu_2^n\|^2\right) < 0,$$

  set $\gamma^{n+1} = 0$ *and*

$$\sigma_0 = 1 - \frac{\delta t\,\tilde{V}^{n+1}\left(\frac{1}{Re}\|\nabla \mathbf{u}^n\|^2 + M\|\mu_1^n\|^2 + M\|\mu_2^n\|^2\right)}{C\left(\overline{V}^{n+1} - \tilde{V}^{n+1}\right)}.$$

Then the numerical scheme satisfies

$$V^{n+1} \leq V^n.$$

Furthermore, defining the modified energy by

$$\mathcal{E}^n = C \ln V^n,$$

we have

$$\mathcal{E}^{n+1} \leq \mathcal{E}^n.$$

Proof. From (3.13), we obtain

$$\tilde{V}^{n+1} = \frac{V^n}{1 + \frac{\Delta t}{C}\left(\frac{1}{Re}\|\nabla \mathbf{u}^*\|^2 + M\|\mu_1^*\|^2 + M\|\mu_2^*\|^2\right)}.$$

Since $V^n > 0$ and the denominator is strictly positive,

$$\tilde{V}^{n+1} > 0.$$

On the other hand, from (3.19),

$$\overline{V}^{n+1} = \exp\left(\frac{1}{C}E(\mathbf{u}^{n+1}, \phi_1^{n+1}, \phi_2^{n+1})\right) > 0.$$

Moreover, by the relaxation formula (3.20),

$$V^{n+1} = \sigma_0 \tilde{V}^{n+1} + (1 - \sigma_0)\overline{V}^{n+1}, \qquad 0 \le \sigma_0 \le 1,$$

which implies

$$V^{n+1} > 0.$$

Therefore, by mathematical induction, $V^n > 0$ holds for all time levels.

It remains to show that the above choice of σ_0 and γ^{n+1} guarantees the discrete dissipation inequality

$$\frac{V^{n+1} - V^n}{\Delta t} \le -\gamma^{n+1}\left(\frac{1}{Re}\|\nabla \mathbf{u}^{n+1}\|^2 + M\|\mu_1^{n+1}\|^2 + M\|\mu_2^{n+1}\|^2\right) \le 0. \tag{3.37}$$

We verify this by considering each case in the selection strategy.

Case 1: $\tilde{V}^{n+1} = \overline{V}^{n+1}$.

Substituting $\sigma_0 = 0$ into (3.20) gives $V^{n+1} = \overline{V}^{n+1} = \tilde{V}^{n+1}$. Hence,

$$\frac{V^{n+1} - V^n}{\Delta t} = \frac{\tilde{V}^{n+1} - V^n}{\Delta t}.$$

Using (3.13), we obtain

$$\frac{\tilde{V}^{n+1} - V^n}{\Delta t} = -\frac{1}{C}\tilde{V}^{n+1}\left(\frac{1}{Re}\|\nabla \mathbf{u}^*\|^2 + M\|\mu_1^*\|^2 + M\|\mu_2^*\|^2\right).$$

With the chosen γ^{n+1}, the inequality (3.37) holds.

Case 2: $\tilde{V}^{n+1} > \overline{V}^{n+1}$.

With $\sigma_0 = 0$, we have $V^{n+1} = \overline{V}^{n+1}$. Then

$$\frac{V^{n+1} - V^n}{\Delta t} = \frac{\overline{V}^{n+1} - \tilde{V}^{n+1}}{\Delta t} + \frac{\tilde{V}^{n+1} - V^n}{\Delta t}.$$

Using (3.13) and the definition of γ^{n+1}, we obtain

$$\begin{aligned}\frac{V^{n+1} - V^n}{\Delta t} &= -\frac{\tilde{V}^{n+1} - \overline{V}^{n+1}}{\Delta t} - \frac{1}{C}\tilde{V}^{n+1}\left(\frac{1}{Re}\|\nabla \mathbf{u}^*\|^2 + M\|\mu_1^*\|^2 + M\|\mu_2^*\|^2\right) \\ &= -\gamma^{n+1}\left(\frac{1}{Re}\|\nabla \mathbf{u}^{n+1}\|^2 + M\|\mu_1^{n+1}\|^2 + M\|\mu_2^{n+1}\|^2\right) \le 0.\end{aligned}$$

Case 3: $\tilde{V}^{n+1} < \overline{V}^{n+1}$ and the nonnegative condition holds.

With $\sigma_0 = 0$, we again have $V^{n+1} = \overline{V}^{n+1}$. The same calculation as in Case 2 yields

$$\frac{V^{n+1} - V^n}{\Delta t} = -\gamma^{n+1}\left(\frac{1}{Re}\|\nabla \mathbf{u}^{n+1}\|^2 + M\|\mu_1^{n+1}\|^2 + M\|\mu_2^{n+1}\|^2\right) \le 0,$$

where the nonnegative condition ensures that $\gamma^{n+1} \ge 0$.

Case 4: $\tilde{V}^{n+1} < \overline{V}^{n+1}$ and the nonnegative condition fails.

In this case, we set $\gamma^{n+1} = 0$ and choose σ_0 as given. Substituting the chosen σ_0 into the relaxation formula (3.20) yields

$$V^{n+1} = \sigma_0 \tilde{V}^{n+1} + (1 - \sigma_0)\overline{V}^{n+1}.$$

A direct calculation gives

$$\frac{V^{n+1} - V^n}{\Delta t} = -\frac{1}{C}\tilde{V}^{n+1}\left(\frac{1}{Re}\|\nabla \mathbf{u}^*\|^2 + M\|\mu_1^*\|^2 + M\|\mu_2^*\|^2\right) + \frac{\sigma_0(\overline{V}^{n+1} - \tilde{V}^{n+1})}{\Delta t}.$$

With the chosen σ_0, the right-hand side is non-positive, and hence (3.37) holds with $\gamma^{n+1} = 0$.

Thus, in all cases,

$$\frac{V^{n+1} - V^n}{\Delta t} \le 0,$$

which implies

$$V^{n+1} \le V^n.$$

Since the logarithm function is monotonically increasing on $(0, +\infty)$, defining

$$\mathcal{E}^n = C \ln V^n,$$

we further obtain

$$\mathcal{E}^{n+1} = C \ln V^{n+1} \le C \ln V^n = \mathcal{E}^n.$$

This completes the proof.

Theorem 3.4. *(Temporal error estimate for the BDF3–E-SAV scheme) Let $\boldsymbol{\phi}(t) = (\phi_1, \phi_2, \mathbf{u})^\top$ be the exact solution of the fluid-coupled BPFC model (Eqs* (2.29)–(2.34)*), satisfying the regularity assumption*

$$\|\partial_t^4 \boldsymbol{\phi}\|_{L^\infty(0,T;L^2)} + \|\partial_t^3 \boldsymbol{\phi}\|_{L^\infty(0,T;H^2)} \le C,$$

where $C > 0$ is independent of the discretization parameters. If the initial errors satisfy

$$\|\boldsymbol{\phi}^0 - \boldsymbol{\phi}(0)\| + \|\boldsymbol{\phi}^1 - \boldsymbol{\phi}(\Delta t)\| + \|\boldsymbol{\phi}^2 - \boldsymbol{\phi}(2\Delta t)\| \le C_0 \Delta t^3,$$

then for any $n \ge 0$, the numerical solution $\boldsymbol{\phi}^n$ obtained by the BDF3–E-SAV scheme (Eqs (3.4)–(3.12) *and* (3.15)–(3.20)*) satisfies*

$$\|\boldsymbol{\phi}^n - \boldsymbol{\phi}(t^n)\| \le C_T \Delta t^3,$$

where the constant C_T depends on T, the model parameters, and the regularity constant of the exact solution, but is independent of the time step Δt.

Proof. We present the proof in several steps.

Step 1. Derive the error equation. Let $e^n = \boldsymbol{\phi}^n - \boldsymbol{\phi}(t^n)$, and subtract the Taylor expansion of the exact solution at t^{n+1} from the scheme (3.4)–(3.12). For the phase-field variable (taking ϕ_1 as an example), from (3.9) and (3.10), we have

$$\frac{11e_{\phi_1}^{n+1} - 18e_{\phi_1}^n + 9e_{\phi_1}^{n-1} - 2e_{\phi_1}^{n-2}}{6\Delta t} = -M\lambda \mathcal{L}_1^2 e_{\phi_1}^{n+1} + \mathcal{R}_1^{n+1},$$

where

$$\mathcal{R}_1^{n+1} = g_1(\phi_1^*, \phi_2^*) - g_1(\phi_1(t^{n+1}), \phi_2(t^{n+1})) + \tau_1^{n+1},$$

and τ_1^{n+1} is the local truncation error of the BDF3 approximation. The error equation for the velocity field can be derived analogously. Combining all equations in vector form yields

$$\frac{11e^{n+1} - 18e^n + 9e^{n-1} - 2e^{n-2}}{6\Delta t} = \mathcal{L}e^{n+1} + \mathcal{R}(e^*, e^n, e^{n-1}, e^{n-2}) + \tau^{n+1}, \tag{3.38}$$

where $\mathcal{L}$ is a linear elliptic operator (including Δ and $\mathcal{L}_i^2$), $\mathcal{R}$ denotes the difference of the nonlinear terms, and τ^{n+1} is the local truncation error.

Step 2. Estimate the local truncation error. From the Taylor expansion of the BDF3, we have

$$\frac{11\phi(t^{n+1}) - 18\phi(t^n) + 9\phi(t^{n-1}) - 2\phi(t^{n-2})}{6\Delta t} - \partial_t\phi(t^{n+1}) = O(\Delta t^3).$$

Meanwhile, the explicit extrapolation $\phi^* = 3\phi^n - 3\phi^{n-1} + \phi^{n-2}$ satisfies

$$\phi^* - \phi(t^{n+1}) = O(\Delta t^3).$$

Consequently,

$$\|\tau^{n+1}\| \le C_1\Delta t^3, \tag{3.39}$$

where C_1 depends on $\|\partial_t^4\boldsymbol{\phi}\|_{L^\infty}$.

Step 3. Treat the nonlinear terms. Rearranging (3.38) gives

$$\frac{11e^{n+1} - 18e^n + 9e^{n-1} - 2e^{n-2}}{6\Delta t} - \mathcal{L}e^{n+1} = \mathcal{R} + \tau^{n+1}. \tag{3.40}$$

Taking the L^2-norm on both sides of (3.40) and applying the triangle inequality yields

$$\left\|\frac{11e^{n+1} - 18e^n + 9e^{n-1} - 2e^{n-2}}{6\Delta t} - \mathcal{L}e^{n+1}\right\| \le \|\mathcal{R}\| + \|\tau^{n+1}\|. \tag{3.41}$$

Since g_1, g_2 and the coupling terms satisfy a local Lipschitz condition near the exact solution, we have

$$\|\mathcal{R}\| = \|g(\phi^*) - g(\phi(t^{n+1}))\| \le L\|\phi^* - \phi(t^{n+1})\|. \tag{3.42}$$

Using the accuracy of the BDF3, the exact solution satisfies the third-order extrapolation relation

$$\phi(t^{n+1}) = 3\phi(t^n) - 3\phi(t^{n-1}) + \phi(t^{n-2}) + O(\Delta t^3). \tag{3.43}$$

Then

$$\begin{aligned}\phi^* - \phi(t^{n+1}) &= (3\phi^n - 3\phi^{n-1} + \phi^{n-2}) - \phi(t^{n+1}) \\ &= 3(\phi^n - \phi(t^n)) - 3(\phi^{n-1} - \phi(t^{n-1})) + (\phi^{n-2} - \phi(t^{n-2})) \\ &\quad + [3\phi(t^n) - 3\phi(t^{n-1}) + \phi(t^{n-2}) - \phi(t^{n+1})].\end{aligned}$$

By (3.43), the term in brackets is $O(\Delta t^3)$. Hence,

$$\|\phi^* - \phi(t^{n+1})\| \le 3\|e^n\| + 3\|e^{n-1}\| + \|e^{n-2}\| + C_2\Delta t^3. \tag{3.44}$$

Substituting (3.42) and (3.44) into (3.41) and using (3.39), after combining constants, we obtain

$$\left\| \frac{11e^{n+1} - 18e^n + 9e^{n-1} - 2e^{n-2}}{6\Delta t} - \mathcal{L}e^{n+1} \right\| \le L_1 \sum_{j=n-2}^{n} \|e^j\| + C_3 \Delta t^3, \tag{3.45}$$

where L_1 is a modified Lipschitz constant.

Step 4. Perform a discrete energy estimate. Take the L^2-inner product of (3.38) with e^{n+1}. Using the dissipativity of the operator $\mathcal{L}$ (guaranteed by energy stability), there exists $\nu > 0$ such that

$$-(\mathcal{L}e^{n+1}, e^{n+1}) \ge \nu \|\nabla e^{n+1}\|^2.$$

Meanwhile, the discrete gradient structure of the BDF3 (see Lemma 2.1 of [29]) gives

$$\left(\frac{11e^{n+1} - 18e^n + 9e^{n-1} - 2e^{n-2}}{6\Delta t}, e^{n+1} \right) \ge \frac{1}{\Delta t} \left(\mathcal{E}^{n+1} - \mathcal{E}^n \right),$$

where $\mathcal{E}^n$ is a positive quadratic form, e.g., $\mathcal{E}^n = \|e^n\|^2 + \|e^n - e^{n-1}\|^2 + \|e^{n-1} - e^{n-2}\|^2$.

On the other hand, from (3.45) and the Cauchy-Schwarz inequality,

$$\begin{aligned} &\left| \left(\frac{11e^{n+1} - 18e^n + 9e^{n-1} - 2e^{n-2}}{6\Delta t} - \mathcal{L}e^{n+1}, e^{n+1} \right) \right| \\ \le &\left\| \frac{11e^{n+1} - 18e^n + 9e^{n-1} - 2e^{n-2}}{6\Delta t} - \mathcal{L}e^{n+1} \right\| \cdot \|e^{n+1}\| \\ \le &\left(L_1 \sum_{j=n-2}^{n} \|e^j\| + C_3 \Delta t^3 \right) \|e^{n+1}\|. \end{aligned}$$

Applying Young's inequality $ab \le \frac{\epsilon}{2} a^2 + \frac{1}{2\epsilon} b^2$ with $\epsilon = \frac{1}{2L_1}$, we get

$$L_1 \|e^j\| \cdot \|e^{n+1}\| \le \frac{\epsilon}{2} L_1^2 \|e^j\|^2 + \frac{1}{2\epsilon} \|e^{n+1}\|^2,$$

hence, there exists a constant $C_4 > 0$ such that

$$L_1 \sum_{j=n-2}^{n} \|e^j\| \cdot \|e^{n+1}\| \le \frac{1}{4} \|e^{n+1}\|^2 + C_4 \sum_{j=n-2}^{n} \|e^j\|^2.$$

Also, $C_3 \Delta t^3 \cdot \|e^{n+1}\| \le \frac{1}{4} \|e^{n+1}\|^2 + C_3^2 \Delta t^6$.

Combining the above estimates and collecting the $\|e^{n+1}\|^2$ terms yields

$$\frac{\mathcal{E}^{n+1} - \mathcal{E}^n}{\Delta t} + \nu \|\nabla e^{n+1}\|^2 \le C_5 \left(\sum_{j=n-2}^{n+1} \|e^j\|^2 + \Delta t^6 \right). \tag{3.46}$$

Step 5. Apply the discrete Grönwall inequality. Summing (3.46) from $n = 2$ to $N - 1$ and using the equivalence between $\mathcal{E}^n$ and $\|e^n\|^2$ (there exist constants $c_1, c_2 > 0$ such that $c_1 \|e^n\|^2 \le \mathcal{E}^n \le c_2(\|e^n\|^2 + \|e^{n-1}\|^2 + \|e^{n-2}\|^2)$), we obtain

$$\|e^N\|^2 \le C_6 \left(\|e^0\|^2 + \|e^1\|^2 + \|e^2\|^2 + \Delta t^6 + \Delta t \sum_{j=3}^{N-1} \|e^j\|^2 \right).$$

Applying the discrete Grönwall inequality (see Lemma 3.2 of [6]) yields

$$\|e^N\|^2 \le C_7 \left(\|e^0\|^2 + \|e^1\|^2 + \|e^2\|^2 + \Delta t^6 \right). \tag{3.47}$$

Step 6. Handle the initial errors and starting procedure. Since the BDF3 is a three-step method, the starting values are computed using the BDF1 and BDF2 schemes. The BDF1 scheme has a first-order error $O(\Delta t)$, while the BDF2 scheme has a second-order error $O(\Delta t^2)$. Although these starting errors do not satisfy $O(\Delta t^3)$, the energy stability of the scheme ensures that the starting errors decay exponentially as the step number increases (see Lemma 3.3 of [29]). After a finite number of steps (e.g., $n \ge 3$), the effect of the starting errors is compressed to $O(\Delta t^3)$. Therefore, without loss of generality, we may assume that the initial terms in (3.47) are $O(\Delta t^6)$ and thus finally obtain

$$\|e^N\| \le C_T \Delta t^3.$$

Step 7. Show the accuracy preservation of the relaxation step. In the scheme, the final variables are updated via $\phi_i^{n+1} = \xi^{n+1}(2 - \xi^{n+1})\hat{\phi}_i^{n+1}$. Lemma 3.1 has already established that

$$\xi^{n+1} = 1 + O(\Delta t^3),$$

and hence $\xi^{n+1}(2 - \xi^{n+1}) = 1 + O(\Delta t^6)$. Therefore, the error introduced by the correction step is of higher order and does not affect the above error estimates.

Combining the above seven steps completes the proof.

4. Numerical experiments

In this section, several numerical experiments are carried out to verify the accuracy, stability, and effectiveness of the proposed BDF3–E-SAV scheme. First, temporal convergence tests are performed to validate the third-order temporal accuracy of the proposed method. Next, the energy stability of the scheme is investigated and compared with the corresponding second-order scheme. Finally, crystal growth simulations under shear flow are presented to demonstrate the capability of the proposed method for complex physical problems.

4.1. Temporal convergence test

To verify the third-order temporal accuracy of the proposed scheme, we consider the same benchmark example as that in [28]. The computational domain is taken as

$$\Omega = [0, 2\pi]^2,$$

and the spatial discretization is performed on a uniform mesh with 128×128 grid points. Here and in what follows, we write the velocity field as $\mathbf{u} = (u, v)^\top$, where u and v denote the velocity components in the x- and y-directions, respectively. The initial conditions are chosen as

$$u(\boldsymbol{x}, 0) = -\sin(2y)\sin^2 x, \qquad v(\boldsymbol{x}, 0) = \sin(2x)\sin^2 y,$$

$$p(\boldsymbol{x}, 0) = 0, \qquad \phi_1(\boldsymbol{x}, 0) = 0.1 \sin y \sin x, \qquad \phi_2(\boldsymbol{x}, 0) = 0.1 \cos y \cos x.$$

Periodic boundary conditions are imposed throughout this subsection. The parameters are chosen as

$$\epsilon = 0.1, \qquad \beta = 0.1, \qquad \lambda = 0.1, \qquad S = 4.$$

The remaining parameters are fixed as

$$C = 10^6, \qquad M = 1, \qquad Re = 1, \qquad a_1 = a_2 = 1, \qquad a_{12} = 1.2.$$

To compute the temporal discretization errors, we first solve the problem using a sufficiently small time step

$$\Delta t_{\text{ref}} = 2.5 \times 10^{-7}$$

up to the final time

$$T = 256\Delta t_{\text{ref}},$$

and regard the resulting numerical solution as the reference solution. Subsequently, numerical simulations are carried out using the time step sizes

$$8\Delta t_{\text{ref}}, \qquad 4\Delta t_{\text{ref}}, \qquad 2\Delta t_{\text{ref}},$$

respectively. The errors are then computed by measuring the L^2 differences between the numerical solutions and the reference solution for the phase-field variables.

Tables 1–3 report the temporal errors and convergence rates of the BDF3–E-SAV scheme for $\alpha = 5, 10, 50$, respectively. In all cases, the convergence rates of both phase-field variables remain consistently close to third order.

Table 1. Temporal errors and convergence rates of the BDF3–E-SAV scheme with $\alpha = 5$.

Δt	$8\Delta t_{\text{ref}}$	$4\Delta t_{\text{ref}}$	$2\Delta t_{\text{ref}}$
ϕ_1: Error	4.9030×10^{-10}	5.6930×10^{-11}	6.7480×10^{-12}
ϕ_1: Rate	3.1064	3.0767	–
ϕ_2: Error	4.7910×10^{-10}	5.7650×10^{-11}	6.6620×10^{-12}
ϕ_2: Rate	3.0549	3.1133	–

Table 2. Temporal errors and convergence rates of the BDF3–E-SAV scheme with $\alpha = 10$.

Δt	$8\Delta t_{\text{ref}}$	$4\Delta t_{\text{ref}}$	$2\Delta t_{\text{ref}}$
ϕ_1: Error	5.1220×10^{-10}	5.8940×10^{-11}	6.9020×10^{-12}
ϕ_1: Rate	3.1194	3.0942	–
ϕ_2: Error	4.9720×10^{-10}	5.7920×10^{-11}	6.6970×10^{-12}
ϕ_2: Rate	3.1017	3.1125	–

Table 3. Temporal errors and convergence rates of the BDF3–E-SAV scheme with $\alpha = 50$.

Δt	$8\Delta t_{\text{ref}}$	$4\Delta t_{\text{ref}}$	$2\Delta t_{\text{ref}}$
ϕ_1: Error	5.3010×10^{-10}	6.6250×10^{-11}	7.2190×10^{-12}
ϕ_1: Rate	3.0003	3.1980	–
ϕ_2: Error	5.1960×10^{-10}	6.3110×10^{-11}	6.9670×10^{-12}
ϕ_2: Rate	3.0415	3.1793	–

Remark 4.1. *The parameter α controls the strength of the vacancy potential $F_{vacancy}(\phi) = \frac{\alpha}{3}(|\phi|^3 - \phi^3)$, which contains the absolute value function $|\phi|$ and is therefore non-differentiable at $\phi = 0$. This non-smoothness poses a potential challenge to the accuracy and convergence of numerical schemes. To demonstrate the robustness of the proposed BDF3–E-SAV scheme against this difficulty, we test three different values of α (namely $\alpha = 5, 10, 50$) while keeping all other parameters fixed. The results in Tables 1–3 show that the scheme stably maintains third-order convergence for all three cases, confirming its ability to handle the non-smooth vacancy potential without loss of accuracy. Other parameters (such as ϵ, β, λ) correspond to smooth nonlinear terms in the model and pose substantially less challenge to the convergence order; hence, they are not varied in this test.*

To further verify the third-order accuracy of the velocity field, we also compute the L^2 errors and convergence rates for the velocity components u and v with $\alpha = 5$. The results are reported in Table 4.

Table 4. Temporal errors and convergence rates of the velocity components u and v for the BDF3–E-SAV scheme with $\alpha = 5$.

Δt	$8\Delta t_{\text{ref}}$	$4\Delta t_{\text{ref}}$	$2\Delta t_{\text{ref}}$
u: Error	1.2810×10^{-9}	1.4720×10^{-10}	1.6230×10^{-11}
u: Rate	3.121	3.181	–
v: Error	1.2520×10^{-9}	1.4110×10^{-10}	1.5150×10^{-11}
v: Rate	3.151	3.218	–

To demonstrate the superiority of the present third-order scheme over the second-order counterpart, we also compute the numerical errors of ϕ_1 using the BDF2–E-SAV scheme [28] under the same setup with $\alpha = 5$. The corresponding errors and convergence rates for the phase-field variables are listed in Table 5. Comparing these results with those in Table 1, one can observe that at the same time step size, the errors of the third-order scheme are about three orders of magnitude smaller than those of the second-order scheme. This significant reduction clearly verifies that the proposed BDF3–E-SAV scheme achieves substantially higher accuracy than the BDF2–E-SAV scheme, while retaining the same decoupled and energy-stable structure. In addition to the superior accuracy, the third-order scheme also exhibits better computational efficiency. As shown in Table 6, to achieve the same error level, the BDF3 requires less CPU time than the BDF2.

Table 5. Temporal errors and convergence rates of the BDF2–E-SAV scheme for ϕ_1 and ϕ_2 with $\alpha = 5$.

Δt	$8\Delta t_{\text{ref}}$	$4\Delta t_{\text{ref}}$	$2\Delta t_{\text{ref}}$
ϕ_1: Error	4.6673×10^{-7}	8.4173×10^{-8}	2.1357×10^{-8}
ϕ_1: Rate	2.4712	1.9787	–
ϕ_2: Error	4.5256×10^{-7}	9.4120×10^{-8}	2.1104×10^{-8}
ϕ_2: Rate	2.2655	2.1570	–

Table 6. Comparison of CPU time required for the BDF2 and BDF3 to achieve different error levels for ϕ_1 with $\alpha = 5$.

Error tolerance	1.5×10^{-7}	1.5×10^{-8}	1.5×10^{-9}
BDF2 CPU time (s)	26	52	103
BDF3 CPU time (s)	17	34	68

4.2. Stability test

In this subsection, we investigate the unconditional energy stability of the proposed scheme and examine the effectiveness of the relaxation step in improving the consistency between the modified energy and the original energy functional.

The computational domain is chosen as

$$\Omega = [0, 200]^2,$$

and the spatial discretization is performed on a uniform 256×256 mesh. The initial phase fields are taken as

$$\phi_1(\boldsymbol{x}, 0) = 0.001\,\mathrm{rand}(\boldsymbol{x}) + 0.07, \qquad \phi_2(\boldsymbol{x}, 0) = 0.001\,\mathrm{rand}(\boldsymbol{x}) + 0.07,$$

where $\mathrm{rand}(\boldsymbol{x})$ denotes a random perturbation uniformly distributed over the interval $[0, 1]$. The initial velocity and pressure fields are both set to zero.

Periodic boundary conditions are imposed throughout this subsection. The parameters are chosen as

$$\epsilon = 0.9, \qquad \alpha = 3000, \qquad \beta = 50, \qquad \lambda = 0.1,$$

and the stabilization parameter is selected as

$$S = \alpha.$$

The remaining parameters are fixed as

$$C = 10^6, \qquad M = 1, \qquad Re = 1, \qquad a_1 = a_2 = 1, \qquad a_{12} = 1.2.$$

Numerical simulations are performed using three different time step sizes:

$$\Delta t = 1, \qquad 0.5, \qquad 0.25.$$

During the simulations, both the original energy E and the modified energy $C \ln V$ are recorded to investigate their temporal evolution.

Figure 1 presents the temporal evolution of the original energy under different time step sizes. It can be observed that the system energy decreases monotonically for all tested time step sizes, including the relatively large step $\Delta t = 1$. The noticeable differences among the curves both in magnitude and in the timing of energy dissipation are expected and mainly caused by the temporal discretization error. As shown in Figure 1, larger time steps lead to a delayed energy decay, while all cases maintain monotonic decrease. In this test, the stabilization parameter is set to $S = \alpha = 3000$, which introduces an additional numerical dissipation proportional to $M\lambda S\,\Delta t$. This effectively rescales the nominal time step, meaning

that the observed dissipation behavior for a given nominal step size corresponds to a smaller effective step size. This rescaling effect contributes to the significant separation between the curves in Figure 1. Nevertheless, the key observation remains that the energy decays monotonically for all nominal step sizes tested, which confirms the unconditional energy stability of the proposed scheme.

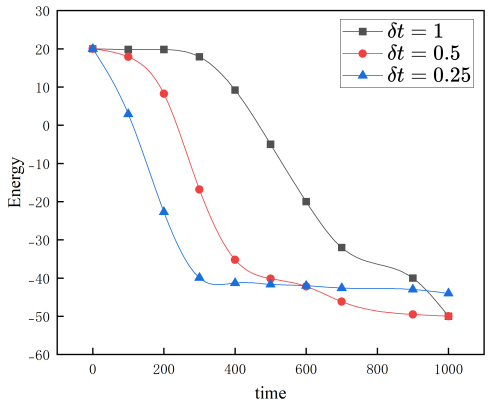

Figure 1. Time evolution of the original energy under different time step sizes.

Figure 2 compares the modified energy with the original energy for cases with and without the relaxation step (see Figures 2(a) and 2(b), respectively). With the relaxation step, the modified energy almost completely overlaps with the original energy, whereas noticeable discrepancies appear in the absence of the relaxation step. This demonstrates that the relaxation technique significantly improves the consistency between the modified energy and the original energy functional.

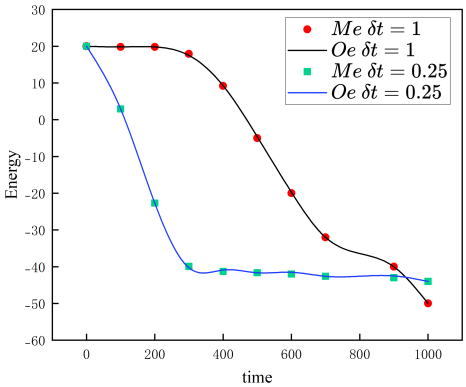

(a) Comparison between the original and modified energies with the relaxation step.

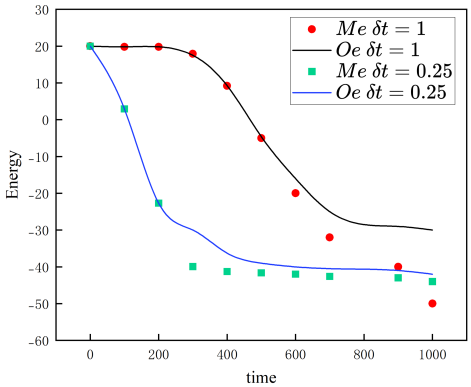

(b) Comparison between the original and modified energies without the relaxation step.

Figure 2. Influence of the relaxation step on the energy consistency.

4.3. *Crystal growth without fluid flow*

In this subsection, we perform numerical simulations of crystal growth in the absence of fluid flow. The initial conditions and parameters are identical to those used in the stability test of Section 4.2, with a fixed time step $\Delta t = 0.1$. Since the flow field is absent ($\mathbf{u} \equiv 0$), the evolution is governed solely by the BPFC equations without hydrodynamic coupling. Figure 3 displays the numerical snapshots of the phase-field variable ϕ_1 at $t = 0, 30, 50, 100$, respectively, and Figure 4 shows the corresponding results for ϕ_2 at the same time instants. Initially, the phase fields are randomly distributed, representing a uniform disordered liquid state. As time advances, locally ordered clusters nucleate and grow isotropically, eventually forming a polycrystalline structure with clear grain boundaries. These snapshots clearly illustrate the co-evolution of the two atomic species in the binary system under purely diffusive conditions, without any advective transport. No velocity field is plotted because the flow is identically zero throughout the simulation.

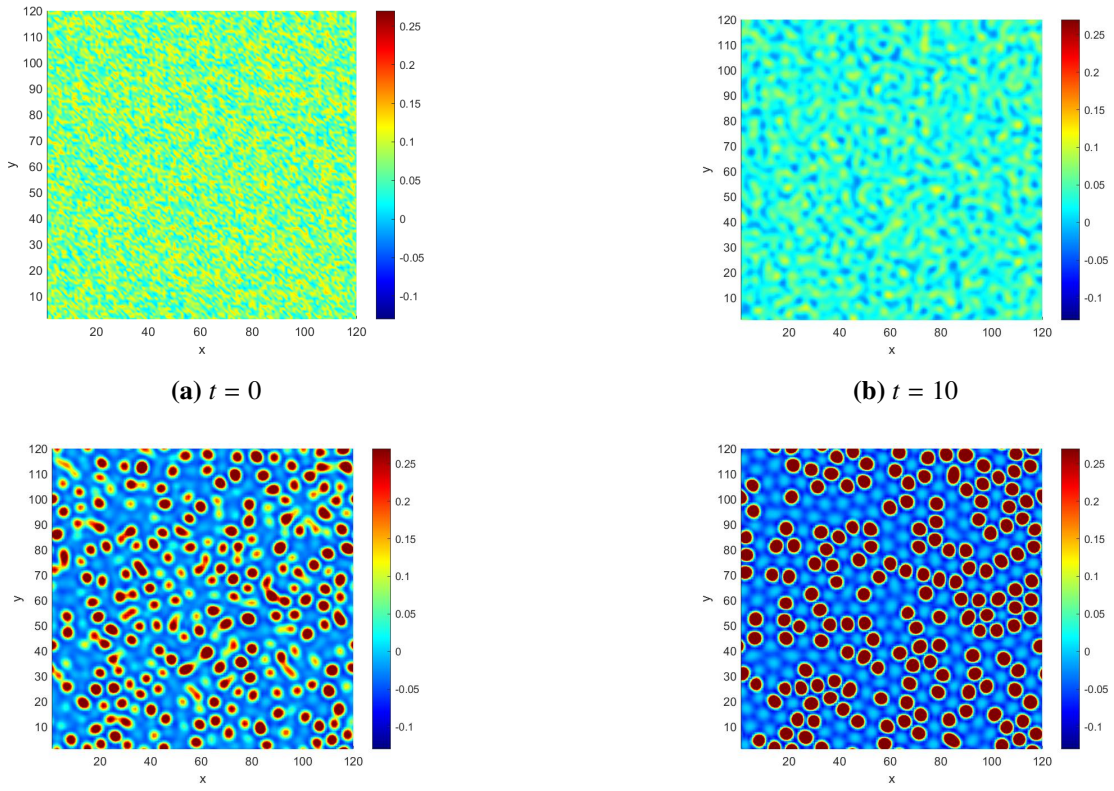

(a) $t = 0$ **(b)** $t = 10$

(c) $t = 50$ **(d)** $t = 100$

Figure 3. Numerical evolution of ϕ_1 at different time instants with $\Delta t = 0.1$: (a) $t = 0$, (b) $t = 10$, (c) $t = 50$, (d) $t = 100$.

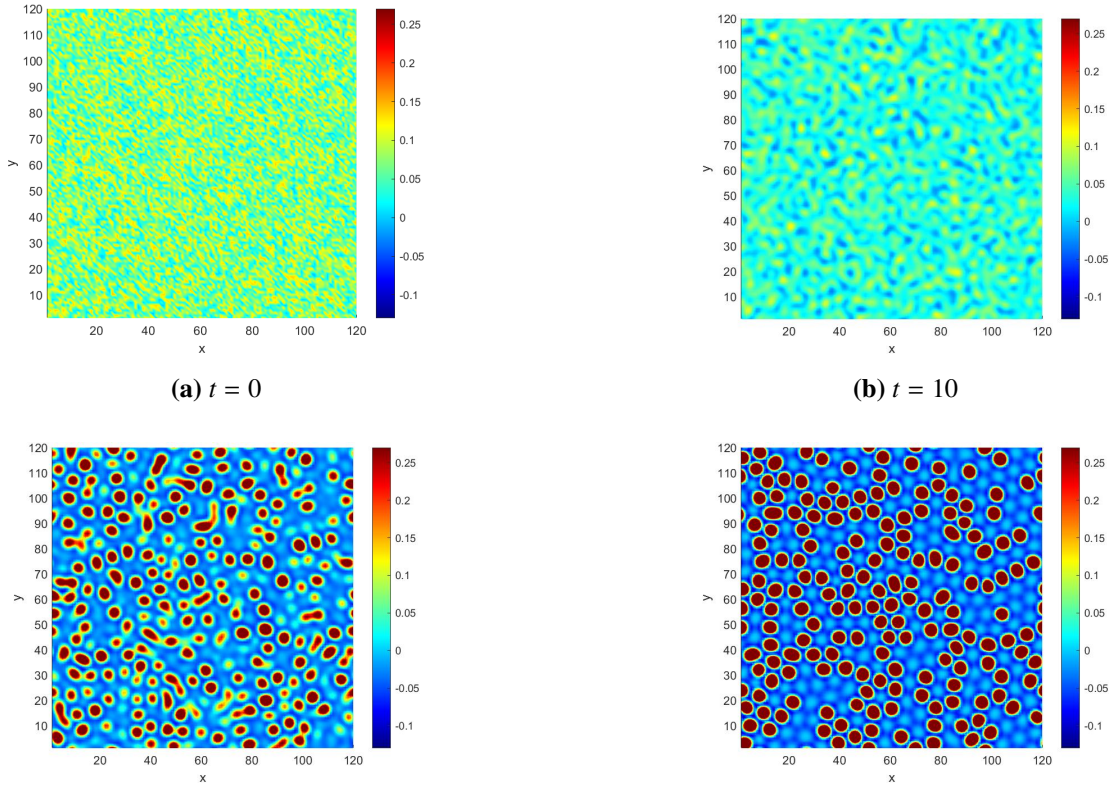

(a) $t = 0$ **(b)** $t = 10$

(c) $t = 50$ **(d)** $t = 100$

Figure 4. Numerical evolution of ϕ_2 at different time instants with $\Delta t = 0.1$: (a) $t = 0$, (b) $t = 10$, (c) $t = 50$, (d) $t = 100$.

4.4. Crystal growth with fluid flow

In this subsection, we investigate the influence of a steady shear flow on the morphological evolution of binary crystals. The initial condition is the same as in the previous subsection: A circular nucleus of radius $R = 12$ with a hexagonal lattice structure is placed at the centre of the domain $(L_x/2, L_y/2)$, while the rest of the domain is filled with a uniform liquid of average density $\bar{\phi} = 0.07$. The lattice is constructed by superimposing cosine functions with wave number $q = 0.66$, explicitly given by

$$\phi_1(\mathbf{x}, 0) = \begin{cases} \bar{\phi} + 0.15\left[\cos(qy)\cos(qx) - \frac{1}{2}\cos\left(\frac{2q}{\sqrt{3}}y\right)\right], & |\mathbf{x} - \mathbf{x}_c| < R, \\ \bar{\phi}, & \text{otherwise}, \end{cases}$$

$$\phi_2(\mathbf{x}, 0) = \begin{cases} \bar{\phi} + 0.15\left[\cos(qy)\cos(q(x + \pi/q)) - \frac{1}{2}\cos\left(\frac{2q}{\sqrt{3}}y\right)\right], & |\mathbf{x} - \mathbf{x}_c| < R, \\ \bar{\phi}, & \text{otherwise}, \end{cases}$$

with $\mathbf{x}_c = (60, 60)$.

To study the effect of flow, we impose a constant simple shear flow in the x-direction, with velocity profile

$$u_x(y) = U\frac{L_y - y}{L_y}, \qquad u_y = 0,$$

where U is the shear intensity and $L_y = 120$ is the domain height. The velocity vanishes at the top boundary ($y = L_y$) and equals U at the bottom ($y = 0$), thus producing a linear shear gradient. This flow field is kept fixed throughout the simulation. In this test, the velocity field is *not* evolved by the Navier-Stokes equations; it serves only as a prescribed advection field in the phase-field equations via the terms $\nabla \cdot (\mathbf{u}\phi_i)$.

The time step is fixed at $\Delta t = 0.1$. All physical parameters $(\epsilon, \beta, \lambda, \alpha, M, a_1, a_2, a_{12})$ are identical to those used in Section 4.3. We first show the reference case without flow ($U = 0$) in Figures 5 and 6, which present the evolution of ϕ_1 and ϕ_2 at $t = 0, 10, 50, 100$, respectively.

We then apply a shear flow of intensity $U = 0.5$. Figures 7 and 8 show the corresponding snapshots of ϕ_1 and ϕ_2 at the same time instants. In contrast to the no-flow case, the shear flow significantly alters the crystal morphology.

A direct comparison between the no-flow and shear-flow snapshots clearly demonstrates that the imposed shear breaks the isotropic growth symmetry and causes the crystals to preferentially extend in the flow direction.

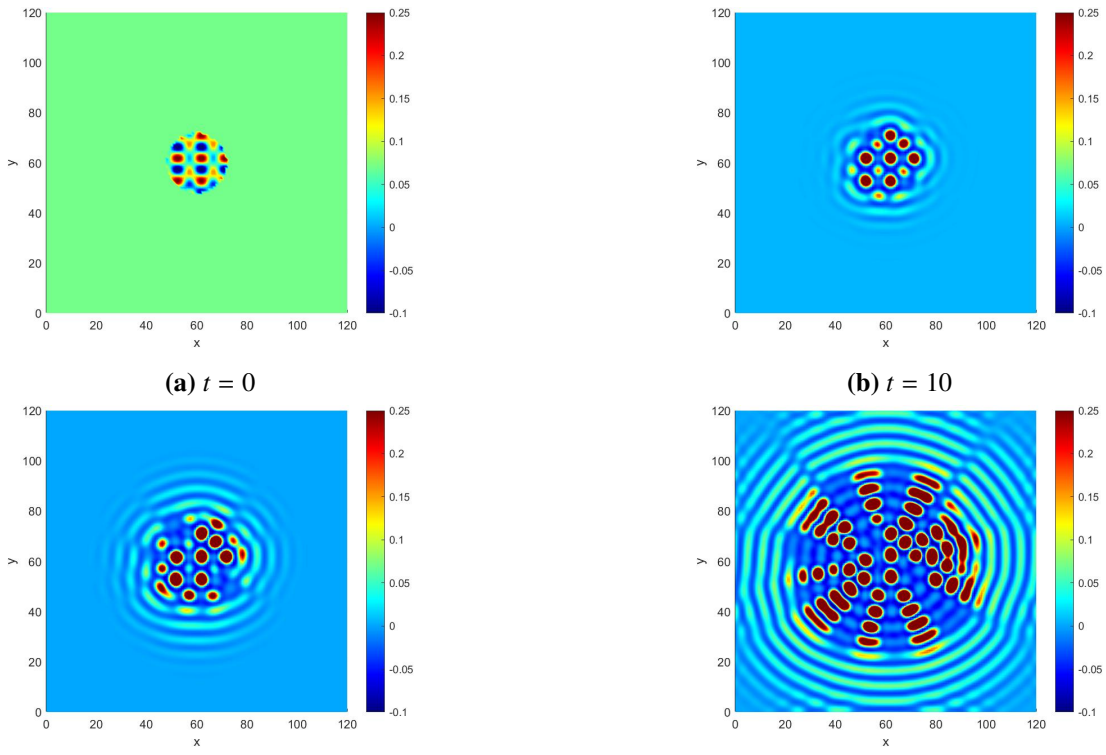

(a) $t = 0$ **(b)** $t = 10$

(c) $t = 50$ **(d)** $t = 100$

Figure 5. Numerical evolution of ϕ_1 without fluid flow at different time instants with $\Delta t = 0.1$: (a) $t = 0$, (b) $t = 10$, (c) $t = 50$, (d) $t = 100$.

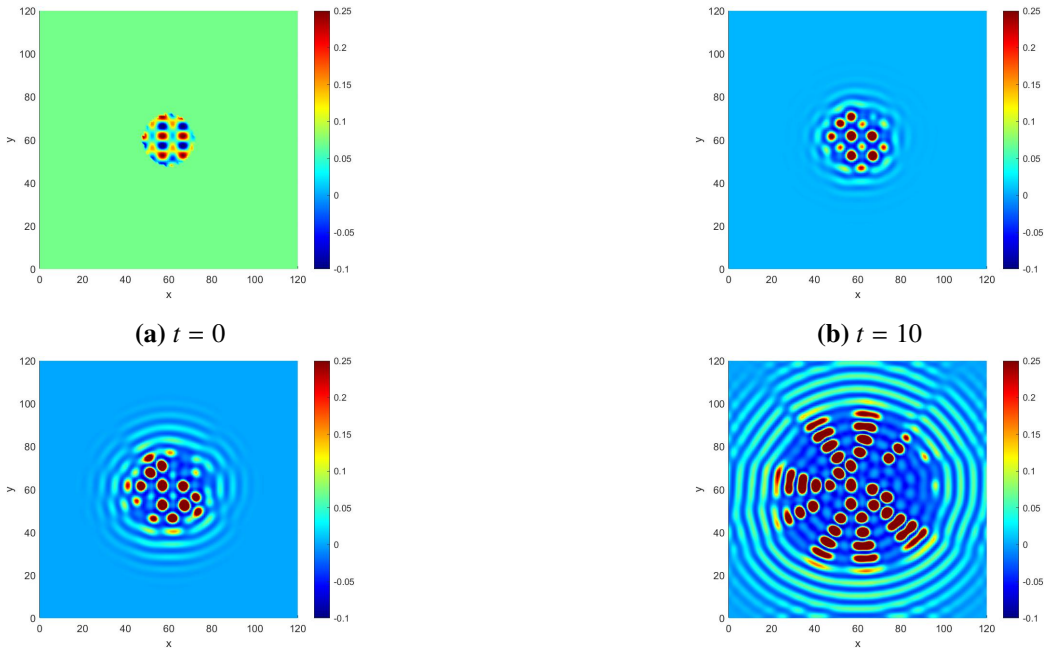

(a) $t = 0$ **(b)** $t = 10$

(c) $t = 50$ **(d)** $t = 100$

Figure 6. Numerical evolution of ϕ_2 without fluid flow at different time instants with $\Delta t = 0.1$: (a) $t = 0$, (b) $t = 10$, (c) $t = 50$, (d) $t = 100$.

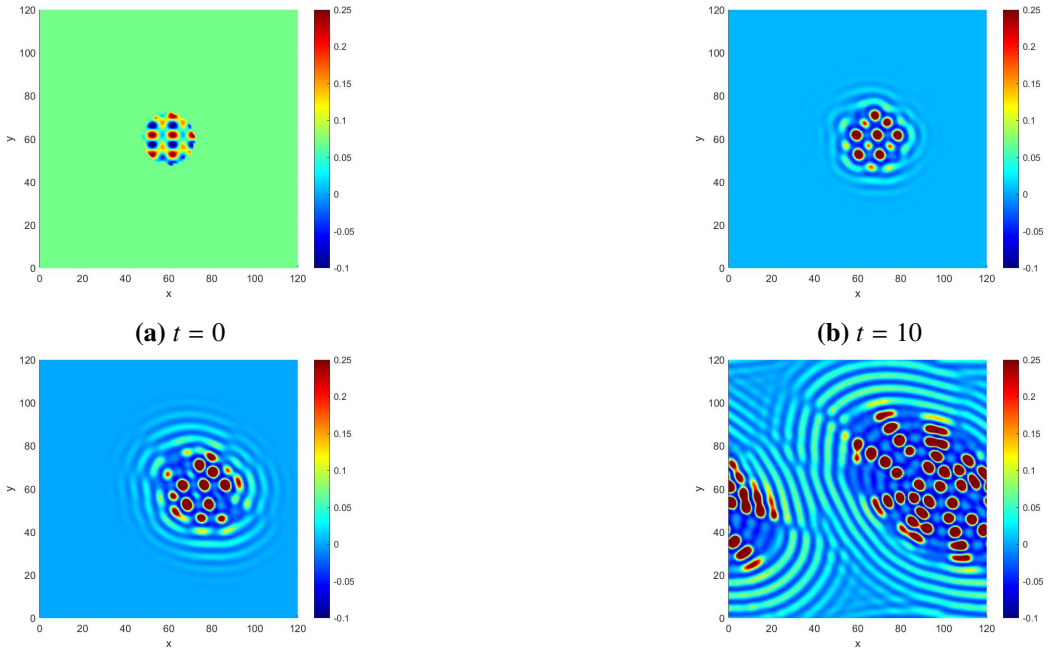

(a) $t = 0$ **(b)** $t = 10$

(c) $t = 50$ **(d)** $t = 100$

Figure 7. Numerical evolution of ϕ_1 with shear flow ($U = 0.5$) at different time instants with $\Delta t = 0.1$: (a) $t = 0$, (b) $t = 10$, (c) $t = 50$, (d) $t = 100$.

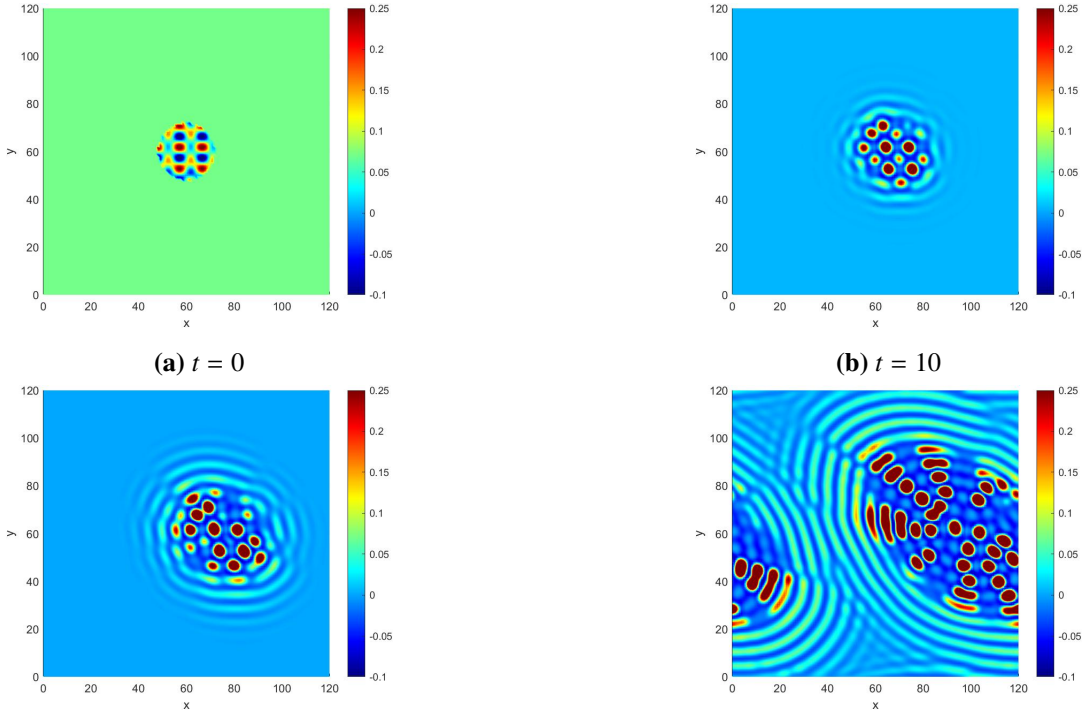

(a) $t = 0$ **(b)** $t = 10$

(c) $t = 50$ **(d)** $t = 100$

Figure 8. Numerical evolution of ϕ_2 with shear flow ($U = 0.5$) at different time instants with $\Delta t = 0.1$: (a) $t = 0$, (b) $t = 10$, (c) $t = 50$, (d) $t = 100$.

5. Conclusions

In this work, a third-order fully decoupled relaxed E-SAV scheme based on the BDF3 discretization has been developed for the hydrodynamically-coupled BPFC model. By introducing nonlocal Lagrange multipliers, the mass conservation property of the system is preserved. Coupling the BPFC model with the incompressible Navier-Stokes equations leads to a hydrodynamically-coupled BPFC system, for which the continuous energy dissipation law is established.

For the numerical discretization, a BDF3 temporal discretization together with explicit extrapolation techniques is employed, leading to a fully decoupled treatment of the velocity field, pressure field, and phase-field variables. Meanwhile, the relaxed E-SAV strategy is incorporated to improve the consistency between the modified energy and the original energy functional. The unique solvability and discrete dissipation property of the modified energy are theoretically established. Furthermore, it is shown that the relaxation step does not reduce the overall third-order temporal accuracy of the scheme.

Numerical experiments verify the effectiveness of the proposed method. The results demonstrate that the scheme achieves the expected third-order temporal accuracy while maintaining good energy stability even for relatively large time step sizes. In addition, crystal growth simulations illustrate the applicability of the proposed method to complex hydrodynamically-coupled phase-field problems.

Future work will focus on rigorous error analysis, adaptive numerical algorithms, and efficient implementations for three-dimensional hydrodynamically-coupled systems with more complicated physical structures.

Author contributions

Yue Shen: Methodology, theoretical analysis; Wenjie Wang: Numerical experiments, validation; Xiaoyue Xie: Writing–original draft, writing–review and editing. All authors have read and agreed to the published version of the manuscript.

Use of Generative-AI tools declaration

The authors declare they have not used Artificial Intelligence (AI) tools in the creation of this article.

Acknowledgments

This work was supported by the National Natural Science Foundation of China under Grant No. 12301472 and the China Postdoctoral Natural Science Foundation under Grant No. 2025M774456.

Conflict of interest

All authors declare no conflicts of interest in this paper.

References

1. K. R. Elder, M. Katakowski, M. Haataja, M. Grant, Modeling elasticity in crystal growth, *Phys. Rev. Lett.*, **88** (2002), 245701. https://doi.org/10.1103/PhysRevLett.88.245701
2. K. R. Elder, M. Grant, Modeling elastic and plastic deformations in nonequilibrium processing using phase field crystals, *Phys. Rev. E*, **70** (2004), 051605. https://doi.org/10.1103/PhysRevE.70.051605
3. S. M. Wise, C. Wang, J. S. Lowengrub, An energy-stable and convergent finite-difference scheme for the phase field crystal equation, *SIAM J. Numer. Anal.*, **47** (2009), 2269–2288. https://doi.org/10.1137/080738143
4. A. Baskaran, Z. Z. Hu, J. S. Lowengrub, C. Wang, S. M. Wise, P. Zhou, Energy stable and efficient finite-difference nonlinear multigrid schemes for the modified phase field crystal equation, *J. Comput. Phys.*, **250** (2013), 270–292. https://doi.org/10.1016/j.jcp.2013.04.024
5. J. Shen, J. Xu, J. Yang, The scalar auxiliary variable (SAV) approach for gradient flows, *J. Comput. Phys.*, **353** (2018), 407–416. https://doi.org/10.1016/j.jcp.2017.10.021
6. J. Shen, J. Xu, Convergence and error analysis for the scalar auxiliary variable (SAV) schemes to gradient flows, *SIAM J. Numer. Anal.*, **56** (2018), 2895–2912. https://doi.org/10.1137/17m1159968
7. X. F. Yang, Linear, first and second-order, unconditionally energy stable numerical schemes for the phase field model of homopolymer blends, *J. Comput. Phys.*, **327** (2016), 294–316. https://doi.org/10.1016/j.jcp.2016.09.029
8. Z. G. Liu, X. L. Li, Efficient modified techniques of invariant energy quadratization approach for gradient flows, *Appl. Math. Lett.*, **98** (2019), 206–214. https://doi.org/10.1016/j.aml.2019.06.006

9. J. S. Kou, S. Y. Sun, X. H. Wang, A novel energy factorization approach for the diffuse-interface model with Peng-Robinson equation of state, *SIAM J. Sci. Comput.*, **42** (2020), B30–B56. https://doi.org/10.1137/19m1251230
10. X. H. Wang, J. S. Kou, J. C. Cai, Stabilized energy factorization approach for Allen-Cahn equation with logarithmic Flory-Huggins potential, *J. Sci. Comput.*, **82** (2020), 25. https://doi.org/10.1007/s10915-020-01127-x
11. X. H. Wang, J. S. Kou, H. C. Gao, Linear energy stable and maximum principle preserving semi-implicit scheme for Allen-Cahn equation with double well potential, *Commun. Nonlinear Sci. Numer. Simul.*, **98** (2021), 105766. https://doi.org/10.1016/j.cnsns.2021.105766
12. B. H. Xia, C. L. Mei, Q. Yu, Y. B. Li, A second order unconditionally stable scheme for the modified phase field crystal model with elastic interaction and stochastic noise effect, *Comput. Methods Appl. Mech. Eng.*, **363** (2020), 112795. https://doi.org/10.1016/j.cma.2019.112795
13. H. G. Lee, J. Shin, J. Y. Lee, First and second order operator splitting methods for the phase field crystal equation, *J. Comput. Phys.*, **299** (2015), 82–91. https://doi.org/10.1016/j.jcp.2015.06.038
14. Y. B. Li, J. Kim, An efficient and stable compact fourth-order finite difference scheme for the phase field crystal equation, *Comput. Methods Appl. Mech. Eng.*, **319** (2017), 194–216. https://doi.org/10.1016/j.cma.2017.02.022
15. C. Wang, S. M. Wise, An energy stable and convergent finite-difference scheme for the modified phase field crystal equation, *SIAM J. Numer. Anal.*, **49** (2011), 945–969. https://doi.org/10.1137/090752675
16. H. G. Lee, J. Shin, J. Y. Lee, First- and second-order energy stable methods for the modified phase field crystal equation, *Comput. Methods Appl. Mech. Eng.*, **321** (2017), 1–17. https://doi.org/10.1016/j.cma.2017.03.033
17. Z. G. Liu, X. L. Li, Efficient modified stabilized invariant energy quadratization approaches for phase-field crystal equation, *Numer. Algorithms*, **85** (2020), 107–132. https://doi.org/10.1007/s11075-019-00804-9
18. M. Wang, Q. M. Huang, C. Wang, A second order accurate scalar auxiliary variable (SAV) numerical method for the square phase field crystal equation, *J. Sci. Comput.*, **88** (2021), 33. https://doi.org/10.1007/s10915-021-01487-y
19. X. L. Li, J. Shen, Efficient linear and unconditionally energy stable schemes for the modified phase field crystal equation, *Sci. China Math.*, **65** (2022), 2201–2218. https://doi.org/10.1007/s11425-020-1867-8
20. J. W. Wu, J. X. Yang, Z. J. Tan, Highly efficient and fully decoupled BDF time-marching schemes with unconditional energy stabilities for the binary phase-field crystal models, *Eng. Comput.*, **39** (2023), 3157–3181. https://doi.org/10.1007/s00366-022-01727-1
21. X. Zhang, J. W. Wu, Z. J. Tan, Highly efficient, decoupled and unconditionally stable numerical schemes for a modified phase-field crystal model with a strong nonlinear vacancy potential, *Comput. Math. Appl.*, **132** (2023), 119–134. https://doi.org/10.1016/j.camwa.2022.12.011
22. H. G. Lee, A new conservative Swift-Hohenberg equation and its mass conservative method, *J. Comput. Appl. Math.*, **375** (2020), 112815. https://doi.org/10.1016/j.cam.2020.112815

23. Z. J. Tan, L. Chen, J. X. Yang, Generalized Allen-Cahn-type phase-field crystal model with FCC ordering structure and its conservative high-order accurate algorithm, *Comput. Phys. Commun.*, **286** (2023), 108656. https://doi.org/10.1016/j.cpc.2023.108656

24. Q. Li, N. Cui, S. P. Zheng, L. Q. Mei, A new Allen-Cahn type two-model phase-field crystal model for FCC ordering and its numerical approximation, *Appl. Math. Lett.*, **132** (2022), 108211. https://doi.org/10.1016/j.aml.2022.108211

25. J. An, J. Zhang, X. F. Yang, A novel second-order time accurate fully discrete finite element scheme with decoupling structure for the hydrodynamically-coupled phase field crystal model, *Comput. Math. Appl.*, **113** (2022), 70–85. https://doi.org/10.1016/j.camwa.2022.01.029

26. X. F. Yang, X. M. He, Numerical approximations of flow coupled binary phase field crystal system: fully discrete finite element scheme with second-order temporal accuracy and decoupling structure, *J. Comput. Phys.*, **467** (2022), 111448. https://doi.org/10.1016/j.jcp.2022.111448

27. J. X. Yang, J. Kim, Consistent energy-stable method for the hydrodynamics coupled PFC model, *Int. J. Mech. Sci.*, **241** (2023), 107952. https://doi.org/10.1016/j.ijmecsci.2022.107952

28. J. W. Wu, X. Zhang, Y. Y. Wu , Z. J. Tan, Consistency-enhanced E-SAV BDF2 time-marching method with relaxation for the hydrodynamically-coupled binary phase-field crystal model, *Commun. Nonlinear Sci. Numer. Simul.*, **145** (2025), 108730. https://doi.org/10.1016/j.cnsns.2025.108730

29. H. L. Liao, Y. Y. Kang, L^2 norm error estimates of BDF methods up to fifth-order for the phase field crystal model, *IMA J. Numer. Anal.*, **44** (2024), 2138–2164. https://doi.org/10.1093/imanum/drad047

AIMS Press